# Lipid packing and cholesterol content regulate membrane wetting by biomolecular condensates

Agustín Mangiarotti[1,*], Kita Valerie Schmidt[1,2], Reinhard Lipowsky[1], Rumiana Dimova[1,*]

[1]Max Planck Institute of Colloids and Interfaces, Science Park Golm, 14476 Potsdam, Germany.
[2]Institute of Biochemistry, Freie Universität Berlin, Thielallee 63, 14195, Berlin, Germany.
*Address correspondence to: Agustin.Mangiarotti@mpikg.mpg.de, Rumiana.Dimova@mpikg.mpg.de

## Abstract

Biomolecular condensates play a pivotal role in cellular processes by interacting with membranes through wetting transitions, leading to mutual remodeling. We investigated how membrane composition, particularly lipid packing, affects condensate wetting using hyperspectral imaging and phasor analysis. Our results show that lipid packing, rather than phase state, determines condensate affinity for membranes. Increasing lipid chain length or cholesterol content enhances lipid packing, thereby decreasing condensate affinity. This regulatory mechanism is consistent across various condensate-membrane systems, underscoring the critical role of the membrane interface. Additionally, protein adsorption promotes extensive membrane remodeling, including tube and double-membrane sheet formation. This work provides a novel mechanism by which membrane composition fine-tunes condensate wetting, highlighting its potential impact on cellular functions and organelle interactions.

## Introduction

The view on intracellular organization expanded with the discovery that in addition to membrane-bound organelles, there are organelles lacking a surrounding membrane, also known as biomolecular condensates. These membrane-less organelles exhibit liquid-like properties and provide additional means of compartmentation, playing key roles in cell physiology and disease[1, 2]. In recent years, several cellular processes involving the interactions between membranes and condensates have been described, such as the biogenesis and fission of protein-rich granules in the endoplasmic reticulum[3, 4], receptor clustering and signaling in T-cells[5, 6], the assembly of endocytic vesicles[7], and the interaction between stress granules and lysosomes[8, 9].

The contact between membrane-bound and membraneless organelles, not only regulates condensate dynamics and assembly[3, 4, 6], but also promotes their mutual remodeling[10, 11, 12, 13, 14, 15, 16], and the transmembrane coupling of phase separated proteins[17]. Studying the mechanism behind such interactions in cells is a challenging endeavor due to the dynamic nature and the small size of condensates, often below optical resolution[14]. In this context, biomimetic systems have been instrumental to overcome these difficulties, enabling the investigation of general mechanisms behind membrane-condensate interactions. At the microscale, wetting transitions govern the interaction between membranes and non-anchored three-dimensional (3D) condensates[18], and can be modulated by different parameters, such as ionic concentration or lipid charge[12, 19]. Advanced microscopy techniques like hyperspectral imaging and fluorescence lifetime imaging microscopy (FLIM) combined with the phasor analysis[20, 21], have allowed to obtain quantitative information on the condensate-membrane interaction at the nanoscale. These approaches revealed a general mechanism by which condensates can locally increase the lipid packing and dehydration depending on their affinity for the membrane[22]. Altogether, these observations constitute the first systematic studies addressing the mechanisms of interaction between condensates and membranes. However, due to the vast diversity of condensates and the different conditions under which they interact, many questions remain unanswered.

We distinguish two classes of membrane-condensate systems extensively explored in the literature. In the first one, the protein molecules are tethered to the membrane trough specific lipid binding such as with NTA (Ni-nitrilotriacetic-acid) lipids, and liquid-liquid phase separation (LLPS) takes place at the membrane surface, producing two-dimensional (2D) condensates[13, 23]. This association allows the condensate to colocalize with a specific lipid phase (domain) in phase separated membranes[6]. In the second class, in which bio(macro)molecules form three-dimensional (3D) condensates on their own, the association with a specific lipid phase can also be driven via a lipid anchor[24]. For example, model polymer-based condensates formed through LLPS of solutions of polyethylene glycol (PEG) and dextran (also known as aqueous two-phase system, or ATPS) have been shown to induce phase separation in membranes containing PEGylated lipids as tethers[24, 25, 26]; the wetting by the droplets was found to lead to vesicle budding and lateral redistribution of the lipids that matched the droplet-induced

budding pattern [26]. In addition, it has been suggested that the lipid phase state drives the phase specific binding of non-tethered 3D condensates[27]. Some studies show that organization in the membrane is altered by interactions with crowded solutions of proteins and polymers due to changes in the activity of the interfacial water[28, 29]. However, a systematic evaluation of the effect of membrane packing on condensate-membrane interactions and how membrane organization influences wetting by biomolecular condensates is missing.

To address this, here we evaluated the effect of lipid chain length and cholesterol content on the interactions with non-tethered 3D condensates. To assess the membrane fluidity, we utilized LAURDAN, a lipid-like fluorescent dye sensitive to polarity changes and water dipolar relaxation in the membrane, designed over forty years ago by Weber and Farris[30, 31]. To date, LAURDAN remains one of the most sensitive fluorescent probes for detecting changes in membrane packing and hydration, and it is extensively used in both *in vitro* and *in vivo* studies[32]. Traditionally, LAURDAN spectral changes in membranes have been quantified using a ratiometric analysis of the two main emission bands, known as generalized polarization (GP), providing a measure for the physical state of the membrane[31, 32, 33].

In the last decade, the spectral phasor approach, which involves taking the Fourier transform of the whole spectrum[34], has further exploited the properties of LAURDAN, broadening its applications for microscopy and cuvette experiments[20, 21, 22, 32, 35, 36, 37]. We combined hyperspectral imaging with the phasor analysis to quantify changes in membrane fluidity. Using microscopy images and theoretical analysis, we derived the condensate affinity for the membrane and the membrane interfacial tensions.

Our findings demonstrate that, in the absence of specific interactions or tethers, lipid packing regulates the wetting affinity of condensates. Increasing lipid chain length, or cholesterol content decreases the condensate-membrane interaction. This mechanism also drives the condensate interaction specificity for a given phase in phase-separated membranes. Moreover, the protein affinity for the membrane can induce the formation of tubes and double membrane-sheets by altering the membrane spontaneous curvature. Extending our results to different condensate systems, suggests that membrane order can generally regulate wetting by biomolecular condensates.

## Results

### 1. Utilizing LAURDAN spectral phasors to finely measure membrane packing changes

Hyperspectral Imaging (HSI) is a microscopy technique that captures a stack of images where each pixel contains spectral information. These data can be analyzed using the spectral phasor approach, which applies a Fourier transform to produce a vector (phasor) for each pixel in a polar plot called the spectral phasor plot[34]. The angular position of the phasors corresponds to the center of mass of the emission spectra, while the radial position relates to the spectral width[38].

Figure 1A shows spectra for LAURDAN in DOPC, DLPC and DPPC giant unilamellar vesicles (GUVs), acquired with HIS at room temperature (23°C). These phospholipids share the same polar headgroup (phosphocholine) but differ in hydrocarbon chain length and saturation: DOPC has two 18-carbon chains with one double bond each, while DLPC and DPPC have saturated chains with 12 and 16 carbons, respectively. This results in membranes with varying degrees of lipid packing and hydration: for the same headgroup, increasing the chain length enhances the van der Waal interactions, reducing the area occupied by each lipid. In Figure 1A it is evident that both the position and shape of the LAURDAN emission spectrum vary with different membrane compositions, as previously reported[28]. The spectrum for DOPC is shifted to longer wavelengths due to the lower degree of lipid packing and the higher water dipolar relaxation. In contrast, for DPPC the membrane is highly packed and exhibits reduced dipolar relaxation as water dynamics around the LAURDAN moiety is limited[31]. The DLPC spectrum falls between these extremes, with an intermediate degree of lipid packing and hydration, as expected [33, 39]. While DOPC and DLPC are in the fluid phase ($L_\alpha$) at 23°C, below their melting temperatures ($T_m$), DPPC ($T_m$=41°C) is in the gel phase ($L_{\beta'}$). The spectral shift between DPPC and DOPC membranes is almost 50 nm, one of the highest reported, highlighting LAURDANs sensitivity to subtle changes in membrane packing and hydration[32, 33, 39].

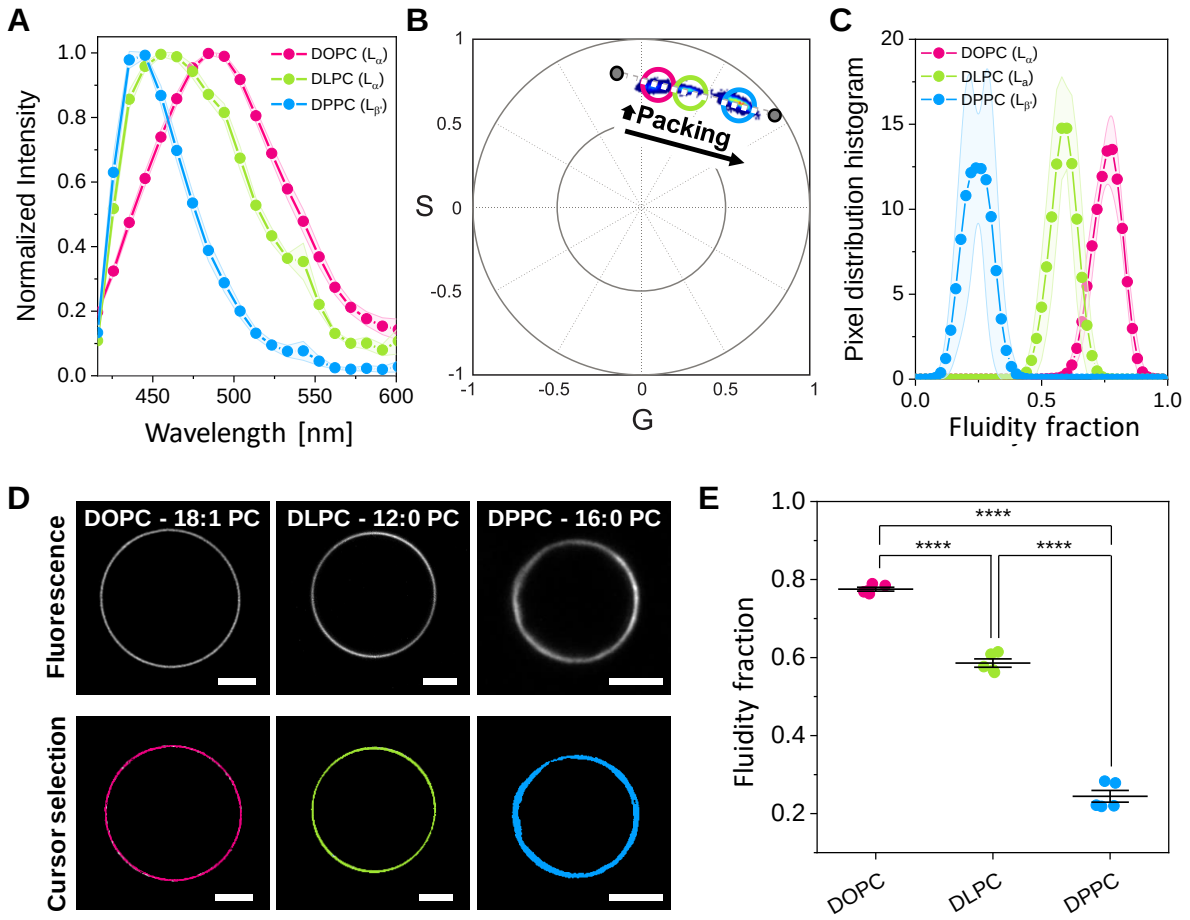


**Figure 1. LAURDAN spectral phasors allow measurement of changes in membrane packing and hydration.** (**A**) LAURDAN spectra reconstituted from hyperspectral imaging of GUVs made of three different lipids. Data are represented as the mean (dots and lines) ± SD (shadowed contour), n = 5 vesicles per condition.

(**B**) Spectral phasor plot for hyperspectral images of DOPC, DLPC, and DPPC GUVs containing 0.5 mol% LAURDAN at (23±1)°C. The plot corresponds to at least five images per condition. Increasing the chain length results in an increase in packing evidenced by the shift of the pixel clouds in a clockwise manner. The pixel clouds are colored according to the pixel density, increasing from blue to red. (**C**) Pixel distribution histograms along the linear trajectory (white dotted line in B), showing the fluidity fraction for the different lipid membranes. Data are represented as the mean (dots and lines) ± SD (shaded area), n = 5 independent experiments per condition. (**D**) Representative confocal microscopy images of GUVs of the indicated lipids (upper panel). Using circular cursors to select the pixel clouds in (B), the corresponding pixels are colored in the images, as shown in the lower panel. Scale bars: 5 µm. (**E**) Center of mass of the histograms shown in (C). Individual data points are shown for each membrane composition. The lines indicate the mean value ± SD.

Figure 1B shows an example of a phasor plot for GUVs made of these different lipids. In this plot, the increased lipid packing is seen as a clockwise displacement of the phasor clouds[21, 35, 36, 40]. Since each pixel in HSI contains spectral information, the phasor transformation results in a pixel cloud with coordinates corresponding to the spectrum shape and position. One advantage of the phasor approach is the ability to exploit the linear algebra of the Fourier space[41]. Due to the linear combination properties of the Fourier space, membranes with varying degrees of packing and hydration form a linear trajectory in the spectral phasor plot, as observed in Figure 3B. The extremes of this trajectory correspond to different surrounding environments for LAURDAN, that reflect the degree of water penetration in the lipid bilayer [32, 36, 40].

It is important to highlight that the changes in polarity due to packing differences and water dipolar relaxation cannot be separated using the LAURDAN spectrum. Therefore, the term “fluidity” is used to describe changes in both parameters [21, 32]. The extremes of the linear trajectory can be defined as the phasor positions for gel and liquid phases, or can be arbitrarily defined, as done here. Using the two-component analysis (see Methods), the pixel distribution along the defined trajectory can be obtained, allowing quantification of differences in the lipid packing and hydration (fluidity), as shown in Figure 1C.

One of the most intriguing features of the phasor approach is the reciprocity principle[21, 42]. This principle allows for selecting pixels in the phasor plot with cursors (as those shown in Figure 1B), which in turn colors the corresponding pixels in the image, as exemplified in Figure 1D. This creates a visual connection between the spatial information and the spectral changes.

To perform statistical analysis on these changes, we calculate the center of mass of the histograms shown in Figure 1C, as shown in Figure 1E. This provides a precise and sensitive measurement of the physical state of the membrane in terms of lipid packing and hydration.

In the following, we utilize LAURDAN spectral phasors to correlate changes in membrane fluidity with the wetting behavior of biomolecular condensates.

## 2. Membrane lipid packing determines the wetting affinity of biomolecular condensates.

Biomolecular condensates have been shown to interact and remodel membranes depending on the salinity and the membrane composition[12, 43, 44]. Wetting by biomolecular condensates can locally

influence membrane packing and hydration, offering a mechanism to modulate membrane properties through regulating the degree of wetting[22]. Here, we investigated whether variations in membrane packing could reciprocally affect condensate wetting under the same buffer conditions. Using glycinin, a soybean protein known to phase separate in response to salinity[45], we examined its interaction with the three different membrane compositions: DOPC, DLPC, and DPPC. All experiments were conducted under identical working conditions: 150 mM NaCl at 23°C, with a protein concentration of 10 mg/mL. Figure 2A illustrates that DOPC membranes exhibit nearly complete condensate spreading, consistent with previous findings[12]. In contrast, DLPC and DPPC membranes display distinct wetting morphologies, underscoring the influence of lipid packing on condensate wetting.

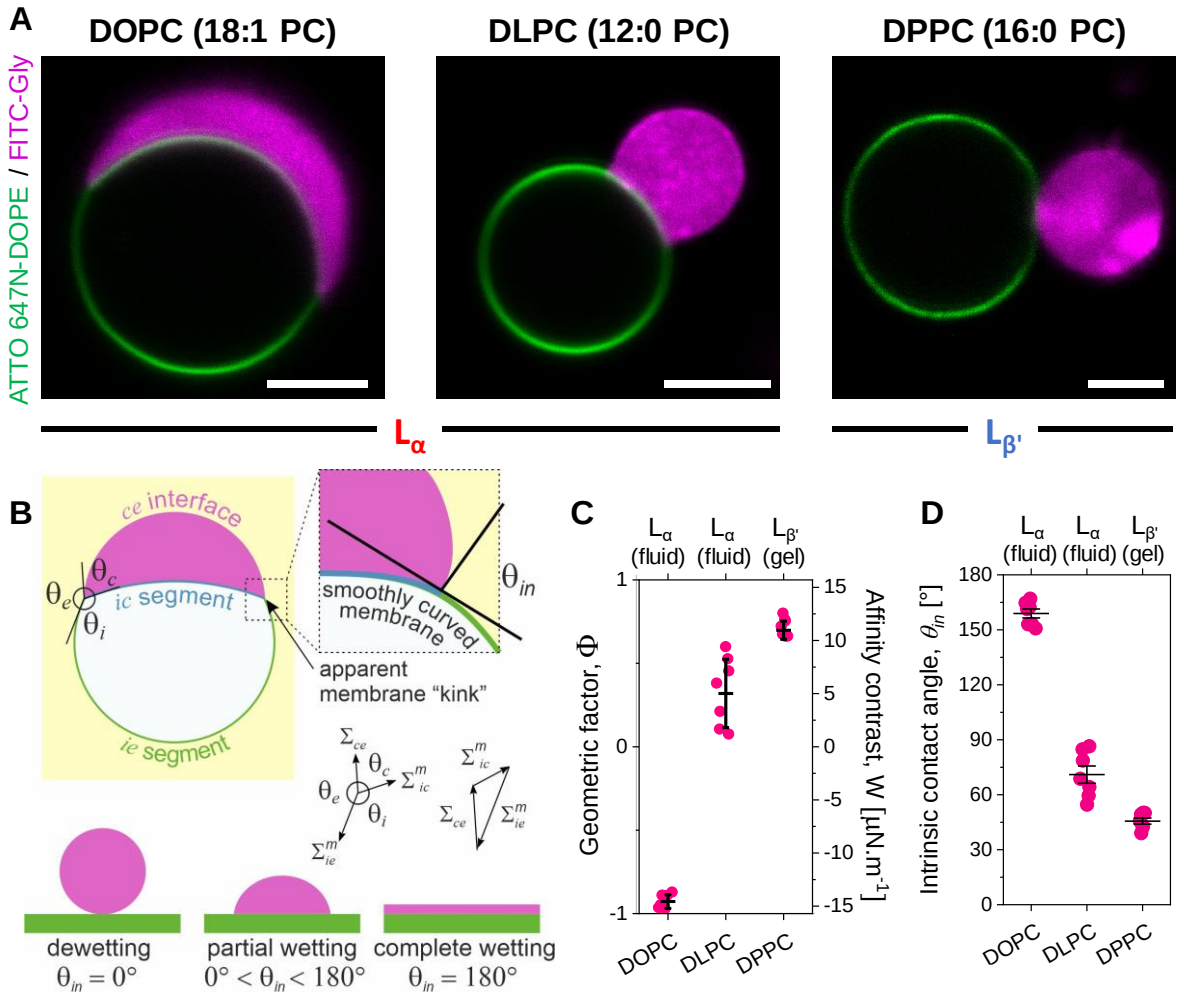


**Figure 2. Membrane packing determines the wetting affinity of biomolecular condensates.** (**A**) Representative confocal microscopy images of GUVs of the indicated lipids labeled with 0.1 mol% ATTO 647N-DOPE (green) in contact with glycinin condensates labeled with FITC-glycinin (magenta) at working conditions (150 mM NaCl, protein concentration 10 mg/mL, 23±1°C). Scale bars: 5 µm. (**B**) Sketch showing the parameters that define the geometric factor (Φ). The three apparent contact angles $\theta_i$, $\theta_c$, and $\theta_e$ (observed microscopically), facing the vesicle interior (*i*), the external solution (*e*) and the condensate (*c*), are related to the three interfacial tensions occurring in the system, $\Sigma_{ce}$, $\Sigma_{ie}^m$, and $\Sigma_{ic}^m$. The three tensions are balanced at the three-phase contact line (black circle) forming the sides of a triangle [43, 46], as shown on the right. At the nanoscale, the membrane is smoothly curved and wetting is characterized by the intrinsic contact angle ($\theta_{in}$). The value of $\theta_{in}$ varies between 0° and 180° depending on the affinity of the condensate droplet for the membrane, as shown in the bottom in analogy to the behavior of liquid droplets at solid substrates. (**C**) Geometric factor (Φ =

$(\sin\theta_e - \sin\theta_c)/\sin\theta_i$, left axis) and affinity contrast ($W = \Sigma_{ce}/\Phi$, right axis) for the different membrane compositions characterizing the affinity of the condensate to the membrane. Individual data points are shown for each membrane composition. The lines indicate the mean value ± SD. (**D**) Intrinsic contact angle $\theta_{in} = \arccos\Phi$ [43, 46] for the different membrane compositions. Individual data points are shown for each membrane composition. The lines indicate the mean value ± SD.

Membrane wetting by biomolecular condensates is quantified by the contact angles formed at the intersection of the two membrane segments and the condensate surface[43, 46], as illustrated in Figure 2B. Note that these contact angles can vary between vesicle-condensate couples and do not reflect the geometry at the nanometer scale, where the membrane is smoothly curved rather than exhibiting a sharp kink[47]; at this scale, wetting is characterized by an intrinsic contact angle $\theta_{in}$ [48], as shown in Fig. 2B. The three apparent microscopic angles, $\theta_i$, $\theta_e$, and $\theta_c$, are related to the three interfacial tensions $\Sigma_{ie}^m$, $\Sigma_{ic}^m$, and $\Sigma_{ce}$, which are balanced at the vesicle-condensate contact line, forming the sides of a triangle (Figure 2B)[46]. This allows us to introduce the geometric factor $\Phi = (\sin\theta_e - \sin\theta_c)/\sin\theta_i$ [12, 43, 46], a dimensionless quantity that depends only on the material properties of the membrane and the condensate; indeed $\Phi = \cos\theta_{in}$[44]. $\Phi$ takes extreme values of $\Phi = 1$ (or $\theta_{in} = 0°$) for dewetting, and $\Phi = -1$ (or $\theta_{in} = 180°$) for complete wetting (see Methods for details)[12, 43]. Figure 2C shows that increasing the degree of lipid packing drives dewetting.

It can be shown [12, 43] that the geometric factor, $\Phi$, is equal to the rescaled affinity contrast, $W/\Sigma_{ce}$, which is a mechanical quantity that describes the different adhesion free energies per unit area of the two membrane segments, see Methods for details. The affinity contrast, W, compares the membrane affinity for the condensate versus the affinity for the protein-poor phase, taking negative values when the membrane prefers the condensate and positive values when it prefers the external buffer. By knowing the condensate interfacial tension $\Sigma_{ce}$, it is possible to assess the affinity contrast, W, which can range from µN to mN. For glycinin condensates under the working conditions, $\Sigma_{ce}$=15.7 µN/m, as determined from rheology and condensate coalescence measurements[22]. Figure 2C shows that the affinity contrast, W, increases when increasing lipid packing, indicating that the membrane prefers the external buffer over the condensate. In Figure 2D, the intrinsic contact angle obtained from the apparent microscopic contact angles is plotted for the different membrane compositions, showing that $\theta_{in}$ decreases for increased packing. Note that, contrary to the observed contact angles, the affinity contrast W, the interfacial tension $\Sigma_{ce}$, the geometric factor $\Phi$, and the intrinsic contact angle $\theta_{in}$, are material parameters, which are independent of the size and shape of the chosen condensate-vesicle couple[11, 12, 43].

### 3. Cholesterol content modulates condensate wetting.

To further demonstrate the influence of lipid packing on interactions with biomolecular condensates, we prepared GUVs with varying cholesterol fractions. Cholesterol impacts several membrane properties, such as lipid packing and hydration[49], permeability and compressibility[50], and bending

rigidity[51]. It is also crucial for forming domains or rafts that promote receptor clustering in cell signaling[6, 52].

Figure 3A shows the phasor plot for LAURDAN in DOPC GUVs with varying cholesterol (Chol) levels. Increasing cholesterol increases lipid packing, again placing the data on a linear trajectory, as expected. Figure 3B-C quantify the fluidity fraction for the DOPC:Chol mixtures. Note that the linear trajectory in Figure 3A aligns with that in Figure 1B, as we fixed the extremes points to allow comparison across different data. The upper panel in Figure 3D displays vesicles colored according to the pixels selected in Figure 3A. Overlapping pixel clouds and circular cursors can cause vesicles to be painted with multiple colors; this should not be confused for domain formation, as all of these mixtures are homogeneous and in the liquid-disordered phase. The lower panel in Figure 3D shows vesicles with different cholesterol content in contact with glycinin condensates. As cholesterol content increases, the condensate affinity for the membrane (wetting) decreases, quantified by the geometric factor and affinity contrast in Figure 3E, and the intrinsic contact angle in Figure 3F.

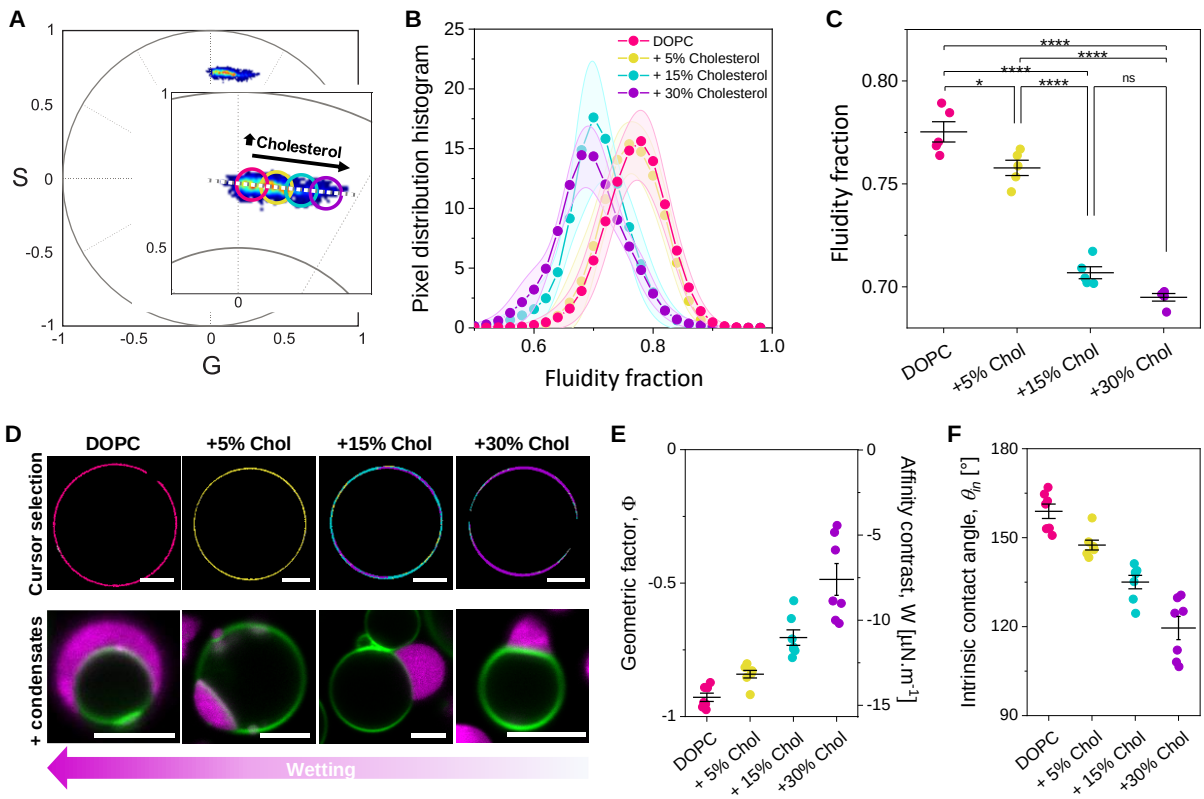


**Figure 3. Cholesterol induced lipid packing modulates condensate wetting.** (**A**) Spectral phasor plot for GUVs made of DOPC and 0%, 5%, 15%, and 30% mol of cholesterol and containing 0.5 mol% LAURDAN at (23±1)°C. (**B**) Pixel distribution histogram along the linear trajectory drawn as a white dotted line in (A), showing the fluidity fraction for the different membrane compositions. Data are represented as the mean (dots and lines) ± SD (shadowed contour), n = 5 independent experiments per condition. (**C**) Center of mass of the histograms shown in (B). Individual data points are shown for each membrane composition. The lines indicate the mean value ± SD. (**D**) Upper panel: cursor colored images of GUVs of the indicated compositions, corresponding to the cursors shown in (A). Lower panel: representative confocal microscopy images of GUVs labeled with 0.1 mol% ATTO 647N-DOPE (green) of the indicated compositions in contact with condensates labeled with FITC-glycinin (magenta) at the working conditions. Scale bars: 5 µm. (**E**) Geometric factor and affinity contrast for condensate/membrane systems at the different membrane compositions. Individual data points are shown for each

membrane composition. The lines indicate the mean value ± SD. (**F**) Intrinsic contact angle for condensate/membrane systems at the different membrane compositions. Individual data points are shown for each membrane composition. The lines indicate the mean value ± SD.

While DOPC:Chol membranes are in the liquid-disordered phase ($L_d$), adding cholesterol to DPPC results in the liquid-ordered ($L_o$) phase. Cholesterol increases membrane packing when mixed with unsaturated lipids like DOPC, as shown in Figure 3, but fluidizes membranes made of saturated lipids like DPPC, as shown in Figure S1, comparing DPPC and DPPC:Chol 70:30. For these compositions, there are no significant differences in condensate wetting, since both the $L_o$ and gel phases are highly packed, and the geometric factor is near the limit for dewetting ($\Phi = 1, \theta_{in} = 0°$).

**4. Lipid packing governs phase-specific interaction in phase-separated membranes.**

The affinity of a condensate for a lipid phase can be modulated by specific tethers for both 2D[6, 53] and 3D[24] condensates. However, for non-tethered 3D condensates (studied here), preferential lipid phase binding has been attributed to the phase state[27], and has been observed as droplet-mediated budding for polymers phase separation inside ATPS GUVs[26]. Above, we demonstrated that condensate affinity can be regulated solely by the membrane packing rather than the phase state, without the need for specific tethers or charges. Fluid ($L_\alpha$) and liquid-disordered ($L_d$) phases showed high and intermediate affinity for the condensates (Figures 2 and 3), while gel ($L_{\beta'}$) and liquid-ordered ($L_o$) phases showed much lower affinity, near dewetting (Figures 1 and S1). To test whether these affinity differences could drive condensate specificity for a given phase in phase-separated membranes, we prepared GUVs of DOPC:DPPC 1:1 displaying fluid/gel phase coexistence ($L_\alpha/L_{\beta'}$), and exposed them to condensates. The fluorescent membrane label (ATTO647N-DOPE) partitions to the fluid phase, making the gel phase appear black in fluorescence microscopy images. Figures 4A,B show that condensates only interact with the fluid phase, avoiding the gel phase. Similarly, in ternary mixtures of DOPC:DPPC:Chol (1:1:1) displaying liquid-disordered/liquid-ordered ($L_d/L_o$) phase separation, condensates only interact with the liquid-disordered phase (Figure 4C,D). Larger field-of-view images (Figure S2) showing several vesicle-condensates pairs confirm that condensates only wet the fluid or liquid-disordered phase, excluding the gel or liquid-ordered phase, respectively, for both binary and ternary lipid mixtures.

The degree of lipid packing (fluidity fraction) of the phases in coexistence explains this behavior, as shown in Figure S3: the fluid phase in the binary mixture is close to DOPC in fluidity, while the gel phase is close to pure DPPC. In the ternary mixture, the liquid-disordered phase has a fluidity fraction between that of DOPC:Chol 7:3 and DLPC, and the liquid-ordered phase lies close to DPPC:Chol 7:3 (Figure S3). These results demonstrate that in the absence of specific tethers or electrostatic interactions, condensate specificity for a given lipid phase is determined by the degree of lipid packing.

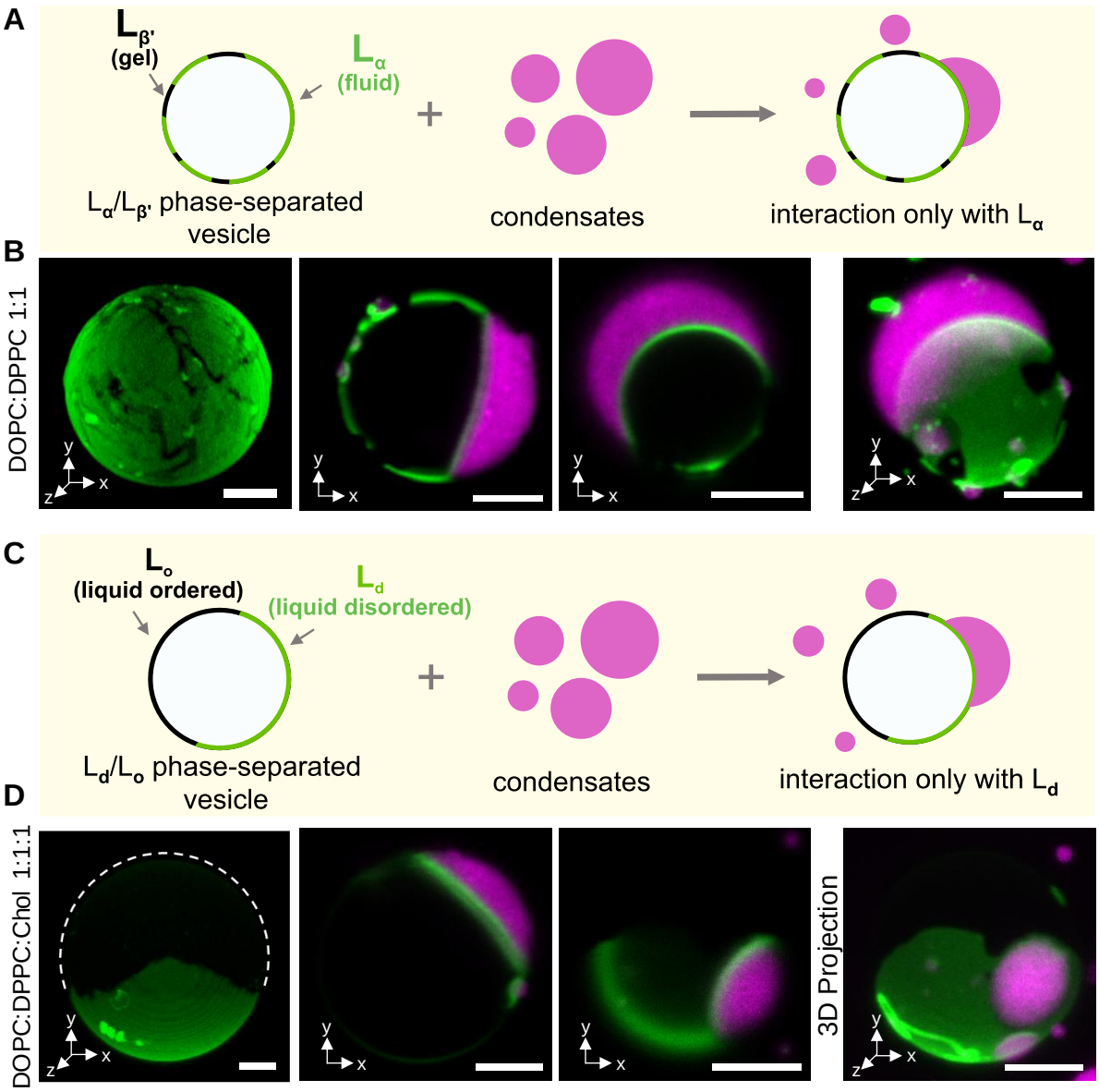


**Figure 4. Lipid packing determines wetting phase specificity in phase-separated membranes.** (**A**) Sketch illustrating that in presence of gel ($L_{\beta'}$) and fluid ($L_{\alpha}$) phases, the condensates bind exclusively to the fluid phase. (**B**) Confocal microscopy images of phase-separated DPPC:DOPC 1:1 GUVs showing that glycinin condensates (magenta) only interact with the fluid phase (green), excluding the gel phase. Images include 2D (x,y) or 3D (x,y,z) projections. The first image shows a vesicle without condensates; the following two images are examples of phase-separated vesicles interacting with condensates, and the last panel is a 3D projection. Scale bars: 5µm. See also Movie S1. (**C**) In the presence of $L_o$ (liquid-ordered) and $L_d$ (liquid-disordered) phases the condensates exclusively interact with the liquid-disordered phase. (**D**) Confocal microscopy images of phase-separated DPPC:DOPC:Chol 1:1:1 GUVs (green) showing that glycinin condensates (magenta) only interact with the liquid-disordered phase (green), excluding the liquid-ordered phase. The white dashed line in the first panel is a guide to the eye indicating the vesicle contour. The middle panels show two confocal examples of condensate interaction with membranes and the last panel is a 3D projection. Scale bars: 5µm. See also Movie S2. All images were taken under the working conditions defined above.

## 5. Membrane remodeling driven by protein adhesion and spontaneous curvature.

Biomolecular condensates can remodel membranes[12, 44], which is crucial in many cellular processes[7, 9, 14]. Glycinin condensates induce interfacial ruffling, forming undulations and finger-like protrusions[12], similar to the "protein pockets" observed in plant tonoplasts[54]. This ruffling depends on the available excess area and can be modulated by tension[12]. Under the working conditions used here, we also observed tubulation. Figure 5A,B show nanotubes forming at the membrane-condensate interface and protruding into the condensate phase (see 3D projections in Fig. S4 and Movies S3 and S4). For DOPC the tube diameters are below the optical resolution (Figure 5A), while the phase separated DOPC:DPPC 1:1 membrane shows pearled-like tubes with dimensions within the optical resolution (Figure 5B). Stimulated emission depletion (STED) super-resolution microscopy reveals average tubes radii of (0.23±0.09) µm for DOPC and (0.43±0.12) µm for DOPC:DPPC 1:1 membranes (Figures 5C and 5D). Note that due to the curved interface, STED images only show tubes in the focal plane; see Movies S5-S6 for STED microscopy z-stacks showing tubes at different planes.

The spontaneous formation of inward tubes has been previously observed in the PEG-rich phase of GUVs encapsulating PEG/dextran ATPS[55, 56]. Tubes nucleate from small buds, grow into necklace-like structures, and can become cylindrical above a critical length[56]. When comparing $L_d$ and $L_o$ membranes, tube diameter depends on the bending rigidity; higher bending rigidity results in higher tube diameter[56].

Here, we observed outward-protruding tubes from the fluid phase of phase-separated DOPC:DPPC 1:1 membranes into the condensates, showing larger diameter than those in pure DOPC. Considering that the fluid phase in DOPC:DPPC 1:1 membranes contain about a 10% of DPPC[57], we measured and compared the bending rigidity of DOPC and DOPC:DPPC 9:1 by fluctuation spectroscopy[58]. We chose this binary mixture because it is homogeneous and approximates the composition of the phase from which the tubes protrude. Figure 5D shows that the bending rigidity of the binary mixture is at least 1.2 times higher than for pure DOPC, which could explain the observed diameter difference.

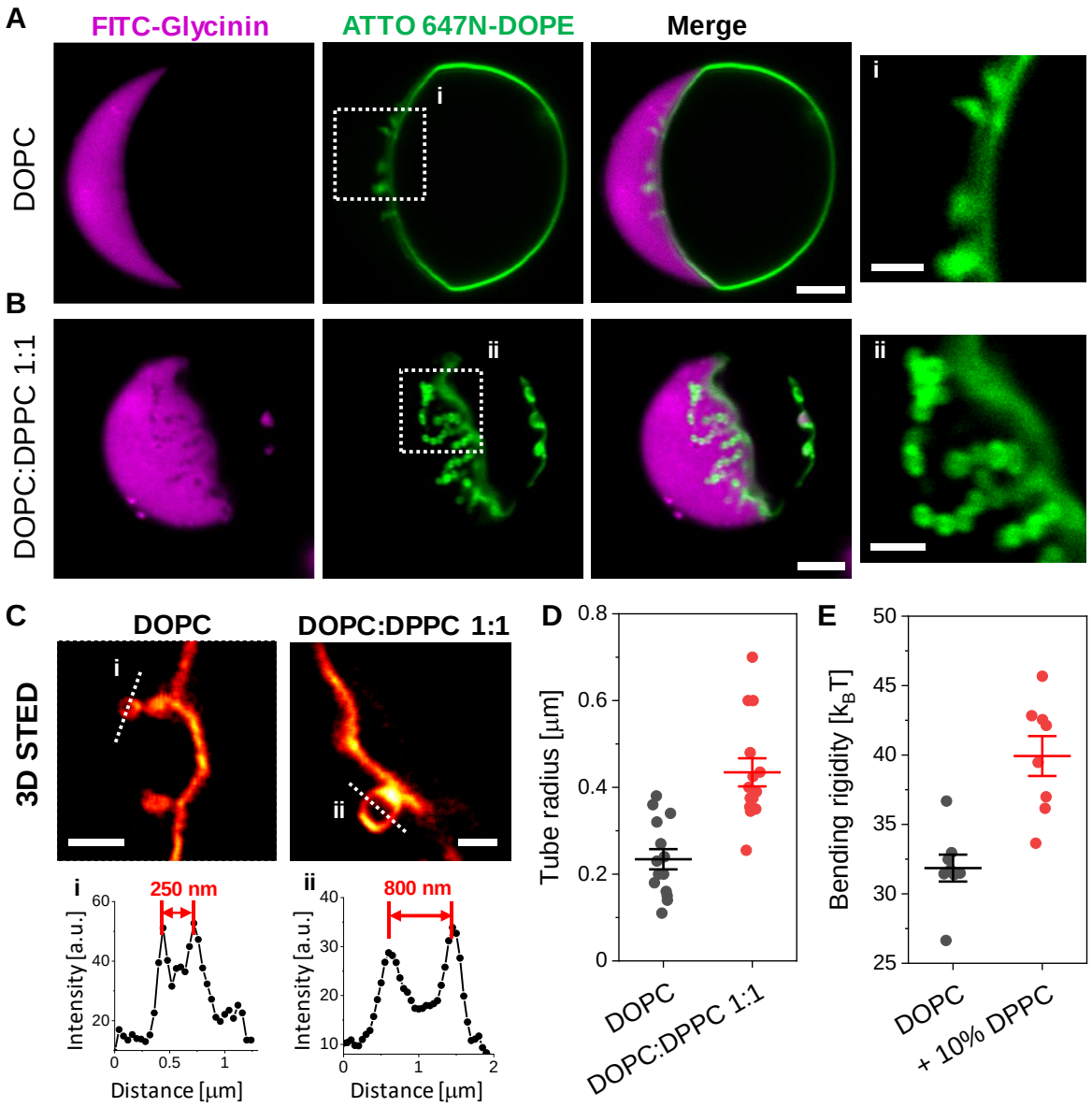


**Figure 5. Nanotubes form at the membrane-condensate interface and their dimensions depend on bending rigidity.** Confocal microscopy images of DOPC (**A**) and DOPC:DPPC 1:1 (**B**) giant vesicles in contact glycinin condensates displaying nanotube formation at the membrane-condensate interface at working conditions. The last panels (i, ii) show the zoomed regions indicated in the membrane channel. Scale bars: 5µm, zoomed images: 2µm. (**C**) 3D STED imaging allows resolving the tube morphology and dimensions. Scale bars: 1µm. (**D**) Tube radius measured from STED images of DOPC and DOPC:DPPC 1:1. (**E**) Membrane bending rigidity measured by fluctuation spectroscopy for DOPC and DOPC:DPPC 9:1. For (D) and (E) individual measurements are shown as dots and the lines indicate mean±SD.

Nanotube formation is generally stabilized by spontaneous curvature[55] that can be triggered by various factors[59]. Since the tubes formed in presence of condensates always protrude into the condensate phase (Figure 5), we tested whether this tubulation was due to spontaneous curvature from protein adsorption. We placed vesicles in contact with glycinin solutions in the homogeneous phase, at low and high salt concentrations away from the binodal. Figure 6A shows the phase diagram for glycinin[45], indicating the conditions for condensate formation (here, 150 mM NaCl) and two homogeneous solutions at low (20 mM) and high (365 mM) NaCl concentrations.

Vesicles were grown in sucrose and then diluted in the corresponding isotonic NaCl (see Methods). In the absence of proteins, this solution asymmetry induces inward tubulation upon deflation[60], see Figure 6B. This result rules out spontaneous curvature from solution asymmetry as the driver for the tubulation observed in Figure 5, since the tubes form in the opposite direction.

To assess the protein effect on the membrane, we prepared vesicles in NaCl under symmetric conditions and added the protein. Figures 6C,D show that glycinin in homogeneous solution adsorbs on the membrane, forming outward buds and tubes. The protein signal at the membrane increases with salinity (Figures 6E) and leads to more extensive tubulation at 365 mM compared to 20 mM NaCl. The increased adsorption at higher salinity aligns with previous observations on affinity of glycinin condensates to membranes[12] and is corroborated by mass photometry data on supported lipid bilayers, showing two-fold increased adsorption as shown in Figure 6F. The latter data, obtained with label-free protein, eliminate potential artifacts related to quantum yield variations in fluorescence intensity measurements and indicate enhanced adsorption at higher salinity. At 20 mM NaCl, glycinin adsorbs predominantly as trimer (160 kDa) and additionally as hexamer (320 kDa), while at 365 mM NaCl it also adsorbs as nonamer (480 kDa) complexes (Figure S5).

Interestingly, we observed that upon extensive tubulation (higher deflation), outward tubes can adhere to the GUVs, form branches over time, and transform into double-membrane sheets (Figure 6G,H). In GUVs encapsulating PEG/Dextran ATPS, nanotubes adsorbed at condensate interfaces have been shown to transform into cisterna-like double-membrane sheets, a wetting driven process, dependent on the interfacial tension and spontaneous curvature[61]. Here, we observe double-membrane sheets adsorbing to the GUV covered by protein rather than to a condensate surface, suggesting that the structures are stabilized by protein-mediated adhesion. Note that both nanotubes and double-membrane sheets adhere to the GUV surface, making them difficult to clearly distinguish from confocal microscopy cross-sections. Visualization of double-membrane sheets requires z-stacks for 3D projections or STED imaging (as shown in Figures 6G and S6, and Movie S7).

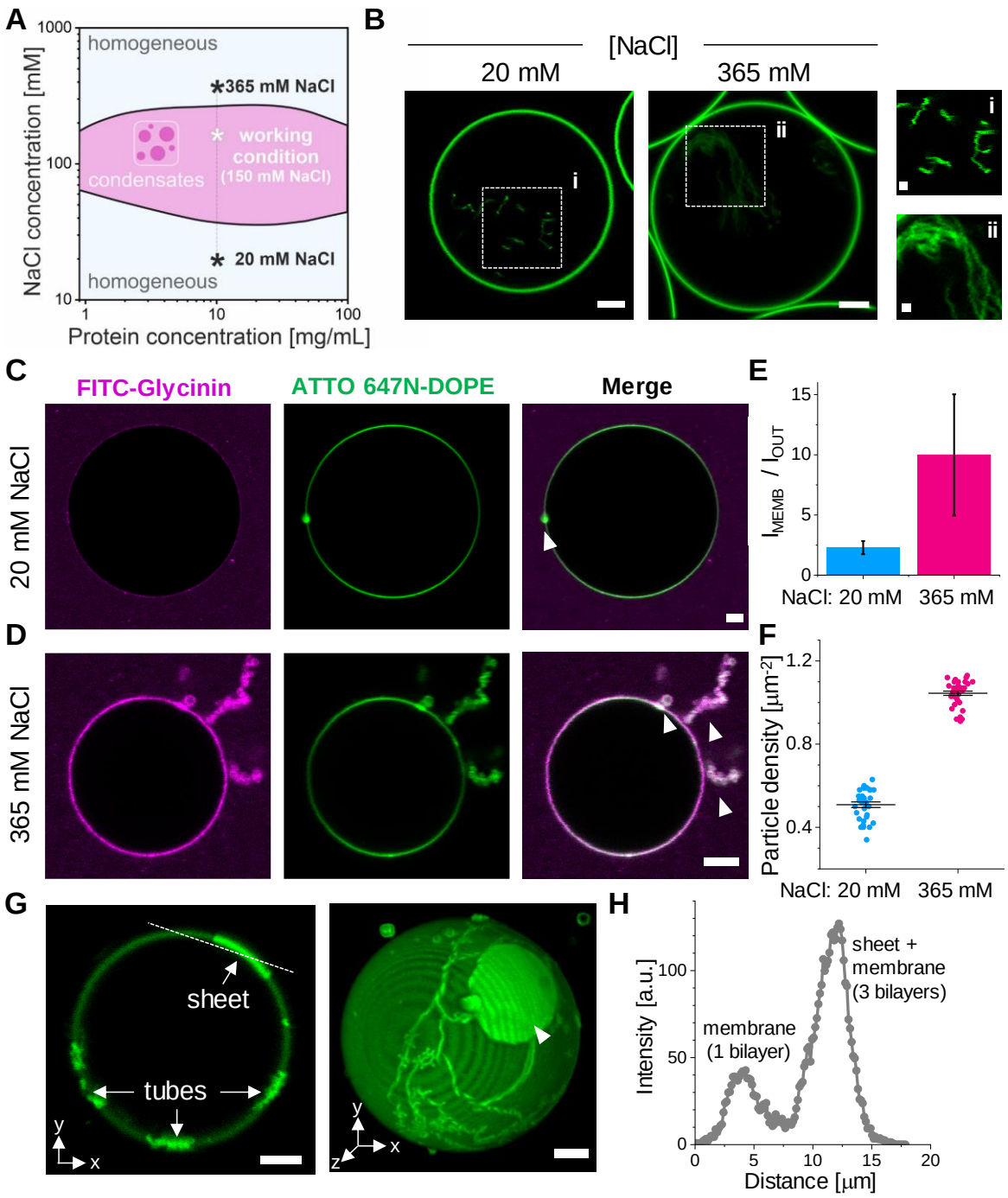


**Figure 6. Protein adsorption drives spontaneous tubulation and mediates double membrane sheet formation.** (**A**) Glycinin phase diagram as a function of NaCl concentration. The working condition for condensate formation, and two homogeneous solutions at low and high salinity are indicated. (**B**) DOPC GUVs grown in sucrose and then diluted in isotonic solutions of the indicated NaCl concentrations show inward tubulation due to the solution asymmetry. Scale bars: 5 µm, zoomed images: 1 µm. (**C-D**) DOPC GUVs grown at 20 mM NaCl (C) or 365 mM NaCl (D) in contact with a homogeneous glycinin solution display outward bud and nanotube formation. Scale bars: 5 µm. (**E**) Ratio of the protein signal intensity (FITC-glycinin) at the membrane ($I_{MEMB}$) to the external solution ($I_{OUT}$), indicating protein binding to the membrane, which increases with higher salinity. (**F**) Particle density obtained by mass photometry for 0.48 µg/mL glycinin solutions at the indicated NaCl concentration, over supported lipid bilayers of DOPC indicating higher adsorption with increasing salinity. (**G**) Confocal microscopy cross-section (left) and 3D projection (right) of the membrane channel for a DOPC GUV in contact with a homogeneous glycinin solution at 365 mM NaCl. The tubes adhere to the vesicle surface and

double-membrane sheet formation is observed. Scale bars: 5 µm. (**H**) Intensity profile across the dashed line shown in G, indicating that the intensity for the double-membrane sheet adsorbed on the vesicle (3 bilayers) is three times higher than for the membrane (single bilayer).

### 6. Correlation between condensates wetting affinity and membrane lipid packing is universal.

To determine whether the dependence of wetting affinity on membrane lipid packing applies broadly, we tested another condensate system with different chemical and material properties than glycinin. The oligopeptides poly-L-lysine ($K_{10}$) and poly-L-aspartic acid ($D_{10}$) form heterotypic condensates at equimolar concentrations, exhibiting low interfacial tension ($\Sigma_{ce}$=17 µN/m) and viscosity (η=80 mPa.s), see Figure S7. In comparison, glycinin condensates, under the conditions shown here, have similar interfacial tension ($\Sigma_{ce}$=15.7 µN/m), but much higher viscosity (η=195 Pa.s)[22].

Previous studies on $K_{10}/D_{10}$ condensates interacting with membranes showed that wetting transitions are achievable by adjusting membrane charge and salinity[12]. Charges in the membrane are necessary for $K_{10}/D_{10}$ condensates[12] to achieve a wetting degree similar to that of glycinin condensates on DOPC (Figure 2). Thus, we produced GUVs made of DOPC, DLPC, and DPPC, with 10 mol% DOPS (all forming homogeneous membranes) to enhance condensate-membrane interaction.

Figure 7A shows confocal microscopy images of $K_{10}/D_{10}$ condensates interacting with membranes of various compositions. Consistent with glycinin observations, increasing lipid packing reduced $K_{10}/D_{10}$ condensates wetting affinity. The fluidity fraction histograms obtained from the spectral phasor plots (Figure S8) are shown in Figure 7B. Inclusion of the charged DOPS increased membranes fluidity (Figure S9) and reduced the fluidity difference between DOPC and DLPC (compare Figures 1C and 7B).

Figure 7C shows the geometric factor and the affinity contrast, and Figure 7D the intrinsic contact angle for $K_{10}/D_{10}$ condensates wetting different membranes. The data trend aligns with glycinin results: higher membrane packing decreases condensate affinity. The geometric factor for DOPC:DOPS 9:1 and DLPC:DOPS 9:1 is similar due to the reduced fluidity differences of these membrane compositions. These results confirm that the observed correlation between wetting affinity and lipid packing is independent of condensate chemistry and material properties, suggesting a general mechanism by which condensate-membrane interactions can be regulated by tuning lipid packing.

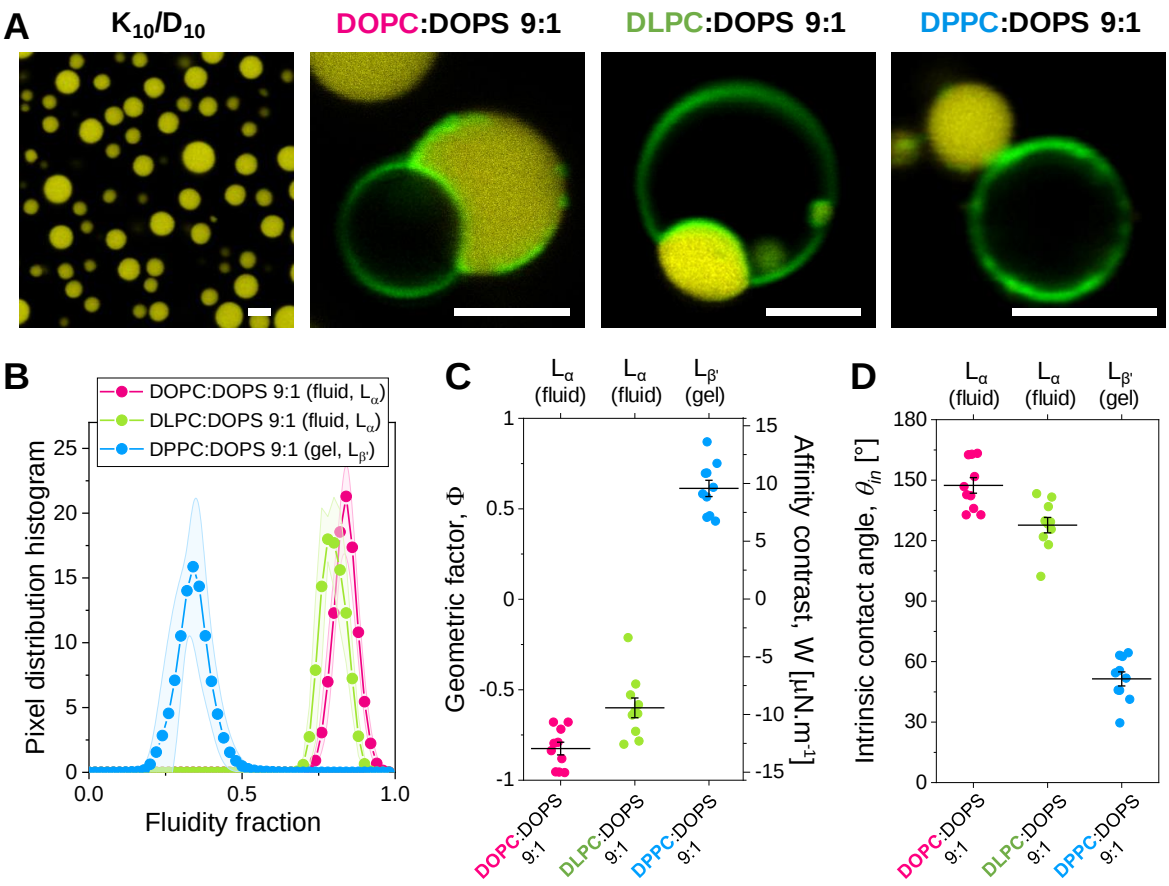


**Figure 7. Influence of lipid packing on condensate wetting is universal across different systems.** (**A**) Confocal microscopy images of $K_{10}/D_{10}$ condensates labelled with 0.1 mol% of TAMRA-$K_{10}$ (yellow), isolated and interacting with GUVs labeled with 0.1 mol% ATTO 647N-DOPE (green) for various membrane compositions. Scale bars: 5 µm. (**B**) Pixel distribution histogram of the fluidity fraction for DOPC, DLPC, and DPPC membranes containing 10 mol% of DOPS; see the phasor plot in Figure S8. (**C**) Geometric factor, Φ, and affinity contrast, $W$, for $K_{10}/D_{10}$ condensates in contact with vesicles of the indicated compositions. (**D**) Intrinsic contact angle $\theta_{in}$ for $K_{10}/D_{10}$ condensates in contact with membranes of the indicated compositions. Individual data points are shown for each membrane composition. The lines indicate the mean value ± SD.

Having established that condensate affinity for the membrane can be tuned through lipid packing, we examined the correlation between fluidity fraction and affinity contrast, $W$, across all tested membrane compositions (with and without cholesterol) in contact with glycinin condensates. Figure 8A demonstrates this direct correlation, which shows an almost linear trend when plotting the intrinsic contact angle against the fluidity fraction, as illustrated in Figure 8B. This further confirms that lipid packing and hydration, rather than membrane phase state, primarily determine wetting interactions.

From the microscopic contact angles defined by the three interfaces shown in Figure 2B and the condensate interfacial tension ($\Sigma_{ce}$), we calculated the tensions of the two membrane segments ($\Sigma_{ie}^{m}$, and $\Sigma_{ic}^{m}$) [43, 46](see Methods). Figure 8C shows these tensions as a function of fluidity fraction for all tested membrane compositions. While the tension for the membrane segment wetted by the condensate, $\Sigma_{ic}^{m}$, decreases with increased fluidity, the tension of the segment wetted by the external buffer, $\Sigma_{ie}^{m}$,

remains approximately constant, regardless of lipid packing. This aligns with previous findings showing that high adhesion energy enables condensates to pull lipids together to the interface[12, 22]. It is important to emphasize that while the affinity contrast $W$ and the intrinsic contact angle $\theta_{in}$ are material properties, the calculated membrane tensions, $\Sigma_{ie}^{m}$ and $\Sigma_{ic}^{m}$, depend on the initial lateral stress of the GUVs, that can vary within the same sample contributing to the observed data dispersion in Figure 8C.

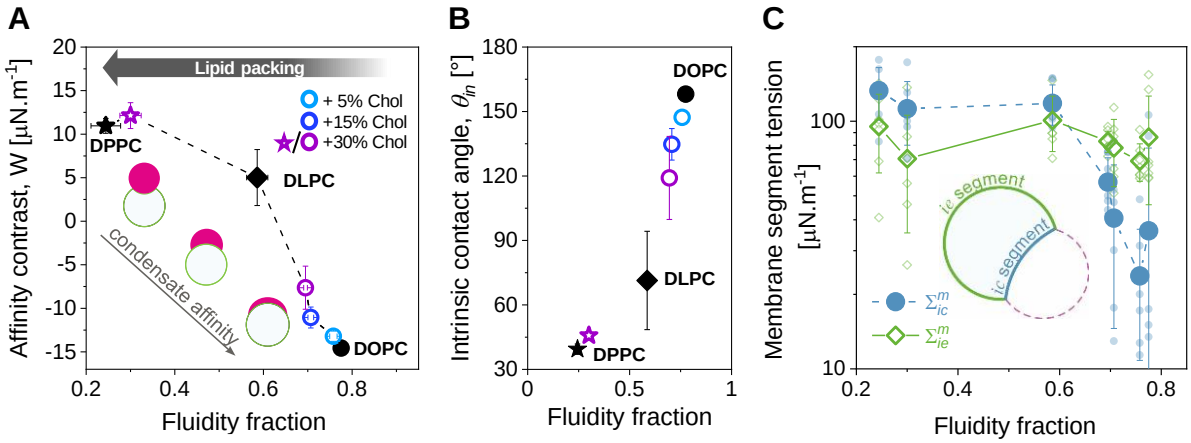


**Figure 8. Membrane fluidity modulates condensate affinity and membrane segment tension.** (**A**) Affinity contrast as a function of fluidity fraction for all tested membrane systems in contact with glycinin condensates. The dashed line is just a guide to the eye. The sketches illustrate that condensate affinity for the membrane increases as $W$ decreases. (**B**) Intrinsic contact angle, $\theta_{in}$ for the same systems shown in A. (**C**) Membrane tension for the $ie$ and $ic$ segments (respectively wetted by the protein-poor phase and by the condensate), as indicated in the sketch. Individual measurements are shown with small symbols and mean ± SD values are indicated with larger symbols. Lines are a guide to the eye. All data were obtained under previously defined working conditions.

## Discussion

Wetting of membranes by biomolecular condensates is a fundamental aspect of organelle interactions crucial to various cellular processes, involved in both, physiology and disease[2, 62]. The elucidation of these interactions has been greatly facilitated by in vitro systems, which allow precise control over physicochemical parameters and reduction of complexity compared to cellular environments[44]. Through such approaches, mechanisms underlying various membrane remodeling processes[12, 13, 18, 63], coupling between membrane and protein phase separation[6, 23, 26, 53], and impact of condensate wetting on membrane order and fluidity[12, 22] have been uncovered, and even revealed new cellular functions of condensates interacting with membranes[9].

In this study, we used hyperspectral imaging and phasor analysis to quantify lipid packing, and derived fluid-elastic parameters from microscopy images, thereby assessing the wetting affinity of condensates for membranes. Our results clearly demonstrate that the degree of lipid packing dictates the wetting affinity. Increasing lipid hydrocarbon chain length or saturation reduces condensate affinity for the membrane (Figures 2 and 7). Additionally, we explored the effect of cholesterol and showed that higher cholesterol levels increase lipid packing and decrease condensate affinity (Figure 3). This effect is

consistent with previous reports indicating that polymer distribution at lipid interfaces is influenced more significantly by fluid than ordered membrane phases[29]. Although we explored model single- or two-component membranes, material properties like bending rigidity and lipid packing have been consistently reproduced in lipid-only membranes, effectively mimicking plasma membranes and extending the applicability of our findings to biological systems[64].

Importantly, our findings show that condensate-membrane interactions are governed by lipid packing rather than membrane phase state per se. For instance, membranes in a fluid phase state (e.g., DOPC and DLPC) exhibit different degrees of packing (Figure 2), and this variability extends to cholesterol compositions (Figure 3), all in the liquid-disordered phase. This suggest that membrane wetting by condensate can be finely tuned through changes in membrane composition.

Condensates wetting influences lipid packing and hydration[22]. Our study reveals that lipid packing, in turn, regulates condensate affinity for the membrane, a phenomenon universal across different condensate systems (Figures 2, 7). This regulatory mechanism is supported by evidence showing that condensate affinity increases with photo-induced membrane area expansion, which reduces packing[65]. These results underscore the crucial role of the lipid interface in mediating the interaction. Considering that the water activity at the interface decreases with increasing lipid packing[29], the dynamics of the interfacial water most likely influences the condensate-membrane interaction. In this sense, the physical state of water has been shown to provide a link between protein structure in bulk and structural changes in lipid membranes[28]. Moreover, cholesterol addition alters the alignment of interfacial water and the membrane dipole potential[66], potentially facilitating the specific association of condensates with cellular organelles of varying cholesterol content[67].

By tethering proteins to the membrane with specific anchors (e.g. NTA lipids, PEGylated or cholesterol-based lipids linked to poly-uridine), it is possible to enhance condensate interaction with specific membrane lipid phases [6, 23, 24, 68]. Our results using non-tethered 3D condensates reveal that lipid packing alone, in the absence of specific interactions, dictates lipid phase specificity (Figure 4).

Condensates are capable of inducing extensive membrane remodeling, including interfacial ruffling, tube formation and double-membrane sheet generation[13, 44, 61, 63, 69]. Here, we observed that protein adhesion promotes the formation of tubular structures at the condensate-membrane interface (Figure 5), facilitated by spontaneous curvature generation (Figure 6). Notably, protein adsorption also drives the formation of double-membrane sheets (Figures 6G-H, S6, Movie S7), reminiscent of processes observed in organelle morphogenesis, such as that of autophagosomes[70] and the endoplasmic reticulum network of interconnected membrane tubes and sheets[71].

In summary, we have unveiled a novel regulatory mechanism by which condensate wetting is modulated, allowing specificity for a distinct lipid phase, whereby both lipid chain length and cholesterol content can influence wetting (Figure 9). The question that remains to be answered is what drives protein binding to the membrane in the absence of tethers, as in the systems presented here. Atomistic and coarse-grained simulations suggest that there is no intercalation of condensate molecules

in the membrane and that electrostatic interactions play an important role[72, 73, 74], even in the absence of charged headgroups[75]. Thus, assessing the electrical properties of condensates is crucial to unraveling their interaction mechanism. The study of membrane-condensate interfaces is challenging, but key to understanding the wetting and remodeling processes orchestrated by condensates.

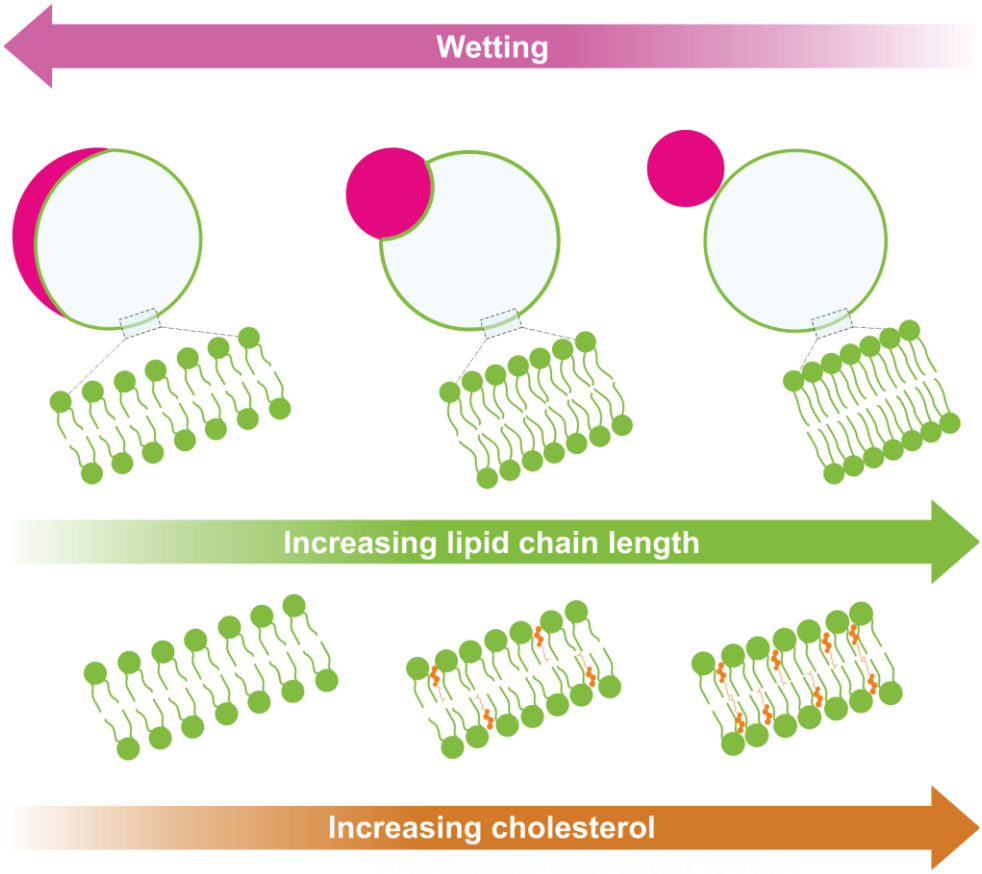


**Figure 9. Sketch summarizing the main findings.** The wetting by biomolecular condensates can be tuned by increasing the membrane lipid packing; this can be achieved increasing the lipid chain length, the degree of chain saturation, or the cholesterol content.

## Materials and methods

### Materials

The lipids 1,2-dioleoyl-sn-glycero-3-phosphocholine (DOPC), 1,2-dilauroyl-sn-glycero-3-phosphocholine (DLPC), 1,2-dipalmitoyl-sn-glycero-3-phosphocholine (DPPC), 1,2-dioleoyl-sn-glycero-3-phospho-L-serine (DOPS), and cholesterol, were purchased from Avanti Polar Lipids (IL, USA). The fluorescent dye 6-dodecanoyl-2-dimethylaminonaphthalene (LAURDAN) was purchased from Thermofisher Scientific (USA). ATTO 647N-DOPE was obtained from ATTO-TEC GmbH (Siegen, Germany). Chloroform obtained from Merck (Darmstadt, Germany) was of HPLC grade (99.8 %). The lipid stocks were mixed as chloroform solutions at 4 mM, containing 0.1 mol% ATTO 647N-DOPE or 0.5 mol% LAURDAN, and were stored until use at -20°C. Fluorescein isothiocyanate isomer (FITC), bovine serum albumin (BSA, fatty acid free), sucrose, glucose, dimethyl sulfoxide (DMSO),

hydrochloridric acid (HCl), sodium hydroxide (NaOH), sodium bisulfite (SBS), sodium chloride (NaCl), potassium chloride (KCl), magnesium chloride ($MgCl_2$), and Polyvinyl alcohol (PVA, MW 145000), were obtained from Sigma-Aldrich (Missouri, USA). The oligopeptides, poly-L-lysine hydrochloride (degree of polymerization, n = 10; $K_{10}$) and poly-L-aspartic acid sodium salt (degree of polymerization, n = 10; $D_{10}$) were purchased from Alamanda Polymers (AL, USA) and used without further purification (purity≥95%). A N-terminal TAMRA-labelled $K_{10}$ was purchased from Biomatik (Ontario, Canada). All aqueous solutions were prepared using ultrapure water from a SG water purification system (Ultrapure Integra UV plus, SG Wasseraufbereitung) with a resistivity of 18.2 MΩ cm.

## Giant vesicle preparation

Giant unilamellar vesicles were prepared by the electroformation method[76], except where indicated. Briefly, 3 µL of the desired lipid solution were spread onto indium tin oxide (ITO)-coated glasses and dried under vacuum for 1 hour. A chamber was assembled using a Teflon spacer and filled with 1.9 mL of the swelling solution. Then, a sinusoidal electric field of 1.0 Vpp and 10 Hz was applied using a function generator for 1 h. For the experiments with condensates, a sucrose solution was used for swelling. In all cases, the solution osmolarities were carefully adjusted using a freezing-point osmometer (Osmomat 3000, Gonotec, Germany).

The GUVs for the experiments in Figure 6, were prepared with the PVA gel-assisted swelling method[77], allowing vesicle swelling in high salinity conditions. Briefly, two coverslips were cleaned with water and ethanol and dried under nitrogen. A 40 mg/mL PVA solution was prepared by heating at 90°C while stirring for 3 h. A 20µL aliquot of the PVA solution was spread on the glass slides and dried for 1 h at 60°C. A 3-4 µL layer of lipid stock solution was deposited on the PVA-coated glass and kept for 1 h under vacuum at room temperature. The chamber was assembled with a 2 mm-thick Teflon spacer and filled with 1 mL of the desired NaCl solution. After 30 minutes, the vesicles were carefully harvested in order to prevent PVA detachment from the cover glass.

In general, vesicles were slightly deflated before the experiments to reduce membrane tension and allow excess area for membrane deformation upon interaction with condensates and protein solutions.

## Preparation of small unilamellar vesicles

Small unilamellar vesicles (SUVs) of pure DOPC were prepared at a total lipid concentration of 500 µM and used for the preparation of supported lipid bilayers. To prepare the SUVs, lipids were dried under vacuum for at least 2 h at room temperature, then resuspended in 1 mL of buffer (20mM Hepes, 150mM KCl, pH 7.4). The glass vial was covered with Parafilm, incubated at 42°C for 30 minutes, vortexed and the content transferred to a 1.5 mL Eppendorf tube. Sonication was performed using a 2 mm tip (Sonopuls MS 72, Bandelin) for 30 min total time, (5% cycle, 20% amplitude) on an ice bath.

The resulting suspension was centrifuged at 21.000 x g for 30 min, and the supernatant containing SUVs was collected.

### Supported lipid bilayer (SLB) formation for mass photometry

Coverslips (24 x 50 mm, Menzel Gläser) were cleaned by alternating spraying isopropanol and Milli Q water for 3x and dried using compressed air. Coverslips were then treated with UV/Ozone (UV/Ozone ProCleaner™, Bio Force Nanosciences) for 20 min.

To form supported lipid bilayers (SLBs) a Silicon gasket (CultureWell™ CW-8R-1.0- Gasket, 8- 6mm diameter x 1mm depth, 15-30µL, Grace Bio-Labs) was placed on a cleaned glass coverslip. 30 µL of SLB buffer (20mM Hepes, 150mM KCl, 1.7mM MgCl2, pH 7.4) was added, followed by 20 µL of SUVs. The mixture was incubated for at least 20 minutes in a home-build humidity chamber. After incubation, the SLB was washed extensively with SLB buffer and the buffer was exchanged to either 20 mM or 365mM NaCl, adjusting the final volume in the well to 60 µL.

A 6.8 µg/mL glycinin stock solution was prepared in either 20 mM or 365mM NaCl. 4.5 µL of this stock solution was added to the well (to a final concentration of glycinin of 0.48 µg/mL) and incubated for 5 minutes before data acquisition.

### Protein extraction, purification, and labeling

Glycinin was purified as described by Chen et al.[45]. Briefly, defatted soy flour was dispersed 15-fold in water by weight and adjusted to pH 7.5 with 2 M NaOH. After centrifugation at 9000×g for 30 min at 4°C, dry sodium bisulfite (SBS) was added to the supernatant (0.98 g SBS/L). The pH of the solution was adjusted to 6.4 with 2 M HCl, and the obtained turbid dispersion was kept at 4 °C overnight. Next, the dispersion was centrifuged at 6500×g for 30 min at 4 °C. The glycinin-rich precipitate was dispersed 5-fold in water, and the pH was adjusted to 7. The glycinin solution was then dialyzed against Millipore water for two days at 4 °C and then freeze-dried to acquire the final product with a purity of 97.5%[45].

To label the protein, 20 mg/mL soy glycinin solution was prepared in 0.1 M carbonate buffer (pH 9). A 4 mg/mL solution of FITC dissolved in DMSO was slowly added to the protein solution with gentle stirring to a final concentration of 0.2 mg/mL. The sample was incubated in the dark while stirring at 23 ºC for three hours. The excess dye was removed using a PD-10 Sephadex G-25 desalting column (GE Healthcare, IL, USA), and the buffer was exchanged with ultrapure water. The pH of the labeled protein solution was adjusted to 7.4 by adding 0.1 M NaOH. For fluorescence microscopy experiments, an aliquot of this solution was added to the working glycinin solution to a final concentration of 4%v/v.

### Formation of glycinin condensates

A 20 mg/mL glycinin solution at pH 7 was freshly prepared in ultrapure water and filtered with 0.45 µm filters to remove any insoluble materials. To form the condensates, the desired volume of the

glycinin solution was mixed with the same volume of a NaCl solution of twice the desired final concentration to a final protein concentration of 10 mg/mL[12, 45].

### Glycinin-vesicles suspensions

Vesicles were diluted 1:10 in a NaCl solution with the final NaCl concentration matching that of the condensates. The condensate suspension was diluted 1:4 and added to the vesicle suspension at a 15% v/v to a final condensate concentration of 0.4 mg/mL. After gently mixing the vesicle-condensate suspension, an aliquot of 100µL was placed on a coverslip (26×56 mm, Waldemar Knittel Glasbearbeitungs GmbH, Germany) for confocal microscopy and a chamber was formed using a round spacer and a closing coverslip. Coverslips were washed with ethanol and water before being passivated with a 2.5 mg/mL bovine serum albumin (BSA) solution.

### Formation of oligopeptides $K_{10}/D_{10}$ coacervates

Phase separation was triggered by gently mixing aliquots of stock solutions of KCl, $MgCl_2$, glucose, $D_{10}$ and $K_{10}$ (in this order) to a final volume of 20 µL. For labeling, a 0.1mol% solution of TAMRA-$K_{10}$ in water was added. The final concentration of each component was: 15 mM KCl, 0.5 mM $MgCl_2$, 170 mM glucose, 2mM $D_{10}$, and 2mM $K_{10}$. The final osmolality of the mixture was ≈ 200 mOsm/kg.

### $K_{10}/D_{10}$-vesicles suspensions

For the interaction of membranes with $K_{10}/D_{10}$ condensates, the vesicle suspension was diluted 1:10 in the final buffer of the corresponding droplet suspension. An aliquot of this diluted vesicle solution was then mixed with the droplet suspension in an 8:1 volume ratio directly on the cover glass and sealed for immediate observation under the microscope.

### Hyperspectral imaging

Hyperspectral images were acquired using a confocal Leica SP8 FALCON microscope equipped with a 63× 1.2 NA water immersion objective (Leica, Mannheim, Germany). The microscope was coupled to a pulsed Ti:Sapphire laser MaiTai (SpectraPhysics, USA), with a repetition rate of 80 MHz. A two-photon wavelength of 780 nm was used for LAURDAN excitation. Image acquisition was performed with a frame size of 512 × 512 pixels$^2$ and a pixel size of 72 nm. For hyperspectral imaging the xyλ mode was used, sequentially measuring in 32 channels with a bandwidth of 9.75 nm in the range 416-728 nm. Hyperspectral images were processed with the SimFCS software developed by the Laboratory of Fluorescence Dynamics, available at https://www.lfd.uci.edu/globals/.

## Spectral phasor plot

LAURDAN fluorescence on hyperspectral imaging data were analyzed using the spectral phasor transform. This analysis calculates the real and imaginary component of the Fourier transform obtaining two quantities that are named G and S. The Cartesian coordinates (G,S) of the spectral phasor plot are defined by the following expressions[21]:

$$G = \frac{\int_{\lambda_{min}}^{\lambda_{max}} I(\lambda) \cos\left(\frac{2\pi n(\lambda-\lambda_i)}{\lambda_{max}-\lambda_{min}}\right) d\lambda}{\int_{\lambda_{min}}^{\lambda_{max}} I(\lambda) d\lambda} \quad (1)$$

$$S = \frac{\int_{\lambda_{min}}^{\lambda_{max}} I(\lambda) \sin\left(\frac{2\pi n(\lambda-\lambda_i)}{\lambda_{max}-\lambda_{min}}\right) d\lambda}{\int_{\lambda_{min}}^{\lambda_{max}} I(\lambda) d\lambda} \quad (2)$$

where for a particular pixel $I(\lambda)$ represents the intensity as a function of wavelength, measured in the interval ($\lambda_{min}$; $\lambda_{max}$). The parameter $n$ is the harmonic, and represents the number of cycles of the trigonometric function that are fit in the wavelength range (here we used $n$=1).

The spectral phasor position of a particular pixel carries information about the spectral intensity profile of that pixel. The spectral center of mass is related to the angle, while the distance from the center carries information on the spectrum broadness.

The spectral phasor approach follows the rules of vector algebra, known as the linear combination of phasors[42]. This property implies that a combination of two independent fluorescent species will appear on the phasor plot at a position that is a linear combination of the phasor positions of the two independent spectral species. The fraction of each component is determined by the coefficients of the linear combination.

## Two-component analysis

The two-component (or two-cursor) analysis was used to exploit the linear combination properties of the phasor plot[42]. It allows to calculate the histogram for the pixel distribution along the linear trajectory (as shown in Fig. 1b) changes in the dipolar relaxation sensed by LAURDAN. When using the term fluidity, we refer to changes in the order of the headgroup-chain interface[78], considering any process that can alter lipid rotational or translational rates. The histograms are presented as the number of pixels at each step along the line between two cursors, normalized by the total number of pixels. We plotted the average value for each histogram ± standard deviation, as well as the center of mass of the histogram for quantitative analysis with descriptive statistics. The center of mass was calculated according to:

$$CM = \frac{\sum_{i=0}^{i=1} F_i\, i}{\sum_{i=0}^{i=1} F_i} \quad (3)$$

where $F_i$ is the fraction for fluidity. Note that independently of the chosen position for the cursors in the phasor plot, the differences between the center of mass of the histograms are determined statistically.

## Contact angles measurement and geometric factor calculation

A detailed explanation of the contact angle measurement and the fluid-elastic parameters used in this work has been published elsewhere[11, 12, 43]. Briefly, the tension triangle in Figure 2b implies the relationships[11]:

$$\frac{\Sigma_{ie}^{m}}{\Sigma_{ce}} = \frac{\Sigma + W_{ie}}{\Sigma_{ce}} = \frac{\sin\theta_c}{\sin\theta_i} \quad \text{and} \quad \frac{\Sigma_{ic}^{m}}{\Sigma_{ce}} = \frac{\Sigma + W_{ic}}{\Sigma_{ce}} = \frac{\sin\theta_e}{\sin\theta_i} \tag{4}$$

between the surface tensions and the contact angles, as follows from the law of sines. Here, $W_{ic}$ and $W_{ic}$ are the respective adhesion parameters of the *ic* and *ie* membrane segments respectively in contact with the condensate and the external buffer (Figure 2B). From the measured contact angles $\theta_e$, $\theta_e$, $\theta_e$, and the condensate surface tension, $\Sigma_{ce}$, it is possible to calculate the tensions of the membrane segments $\Sigma_{ic}^{m}$ and $\Sigma_{ie}^{m}$, as shown in Figure 8B. The affinity contrast, $W$, between the condensate and the external buffer is given by:

$$W \equiv W_{ic} - W_{ie} = \Sigma_{ic}^{m} - \Sigma_{ie}^{m} \text{ with } -\Sigma_{ce} \leq W \leq +\Sigma_{ce} \tag{5}$$

The limiting value $\mathrm{W} = -\Sigma_{ce}$ corresponds to complete wetting by the condensate phase whereas the limiting case $\mathrm{W} = +\Sigma_{ce}$ describes dewetting from the condensate phase. When taking the difference between the two equations in 4, the affinity contrast, W, becomes:

$$W = \Phi\Sigma_{ce} \text{ with } \Phi \equiv \frac{\sin\theta_e - \sin\theta_c}{\sin\theta_i} \tag{6}$$

The rescaled affinity contrast, $W/\Sigma_{ce}$, is a mechanical quantity related to the adhesion free energies of the membrane segments, and is equal to the geometric factor, $\Phi$, that can be obtained from the three contact angles. The inequalities in Eq. (5) imply $-1 \leq \Phi \leq 1$ for the geometric factor, $\Phi$. When $\Phi = -1$ there is complete wetting of the membrane by the condensate phase, while $\Phi = +1$ corresponds to dewetting of the membrane by this phase. The dimensionless factor, $\Phi$ is negative if the membrane prefers the condensate over the exterior buffer and positive otherwise. Note that $\Phi$ is scale-invariant and does not depend on the relative sizes of a given vesicle-condensate couple[12].

Note that to adequately measure the contact angles between the different interfaces from microscopy images, it is necessary that the rotational axis of symmetry of the vesicle-droplet system to lie in the image plane of the projected image. Otherwise, an incorrect projection will lead to a misleading interpretation of the system geometry and incorrect contact angles.

## STED microscopy

An Abberior STED setup (Abberior Instruments GmbH) based on an inverted Olympus IX83 microscope (Olympus Inc., Japan) equipped with a 60×,1.2 NA water immersion objective was used to obtain the super-resolved images. The sample was excited at 640 nm and a 775 nm pulsed beam was used as the depletion laser. Alignment was achieved as described previously for our setup[47]. Briefly, 150 nm gold beads (Sigma-Aldrich, USA) were observed in reflection mode to overlap the center of the excitation focus with the center of the depletion focus. Corrections for mismatches between the scattering and fluorescence modes were performed using 100 nm TetraSpeck™ beads (Invitrogen, USA). To measure the resolving power of the setup, crimson beads of 26 nm diameter (FluoSpheres™, Molecular Probe) were used. A measured resolution of ~35 nm was achieved using 80% STED laser power (total laser power of 1.25 W), improving by 10-fold the lateral resolution of the corresponding excitation laser[47]. For our experiments, 3D STED was more suitable than 2D STED, since we could eliminate the interference of out-of-focus signal coming from the curved regions of the membrane. Images were obtained using a pixel size of 50 nm and a dwell time of 10 µs.

## FRAP measurements

FRAP measurements were performed on the SP8 setup equipped with a FRAP booster. The region of interest (ROI) was circular with a diameter of 2 µm. The condensates were bleached during 3 iterative pulses with a total time of ~3 s. Fluorescence intensities from ROIs corresponding to photobleaching were analyzed using ImageJ.

## Mass photometry data acquisition and analysis

Mass photometry data were acquired using a OneMP instrument (Refeyn Ltd) on a detection area of 10.8 µm × 6.8 µm, at 270 Hz for 30 sec with frame binning set to 2. Data analysis followed the procedure described by Foley *et al.* [79], using the Python scripts provided by the authors with minor adjustments according to the device specifications. Mass calibration was performed in the absence SLB. The particle density was obtained by averaging counted particles per area in each frame.

## Data reproducibility and statistics

At least three independent experiments were used to perform the statistical analysis. Pixel histograms are shown as means ± standard deviation (SD). The center of mass measurements are represented as scatter plots containing the individual measurements and the mean values±SD. Results were analyzed using One-way ANOVA and Tukey post-test analysis ($p<0.0001$, **** | $p<0.001$, *** | $p<0.01$, ** | $p<0.05$, * | ns = non-significant). Statistical analyses and data processing were performed with the Origin Pro software (Originlab corporation). All the microscopy images shown are representative of at least three independent experiments.

## References


1. Banani SF, Lee HO, Hyman AA, Rosen MK. Biomolecular condensates: organizers of cellular biochemistry. *Nature Reviews Molecular Cell Biology* 2017, **18**(5)**:** 285-298.

2. Shin Y, Brangwynne CP. Liquid phase condensation in cell physiology and disease. *Science* 2017, **357**(6357)**:** eaaf4382.

3. Lee JE, Cathey PI, Wu H, Parker R, Voeltz GK. Endoplasmic reticulum contact sites regulate the dynamics of membraneless organelles. *Science* 2020, **367**(6477)**:** eaay7108.

4. Snead WT, Jalihal AP, Gerbich TM, Seim I, Hu Z, Gladfelter AS. Membrane surfaces regulate assembly of ribonucleoprotein condensates. *Nature Cell Biology* 2022, **24**(4)**:** 461-470.

5. Su X, Ditlev JA, Hui E, Xing W, Banjade S, Okrut J, *et al.* Phase separation of signaling molecules promotes T cell receptor signal transduction. *Science* 2016, **352**(6285)**:** 595-599.

6. Wang H-Y, Chan SH, Dey S, Castello-Serrano I, Rosen MK, Ditlev JA, *et al.* Coupling of protein condensates to ordered lipid domains determines functional membrane organization. *Science Advances* 2023, **9**(17)**:** eadf6205.

7. Day KJ, Kago G, Wang L, Richter JB, Hayden CC, Lafer EM, Stachowiak JC. Liquid-like protein interactions catalyse assembly of endocytic vesicles. *Nature Cell Biology* 2021, **23**(4)**:** 366-376.

8. Liao Y-C, Fernandopulle MS, Wang G, Choi H, Hao L, Drerup CM, *et al.* RNA Granules Hitchhike on Lysosomes for Long-Distance Transport, Using Annexin A11 as a Molecular Tether. *Cell* 2019, **179**(1)**:** 147-164.e120.

9. Bussi C, Mangiarotti A, Vanhille-Campos C, Aylan B, Pellegrino E, Athanasiadi N, *et al.* Stress granules plug and stabilize damaged endolysosomal membranes. *Nature* 2023, **623**(7989)**:** 1062-1069.

10. Gouveia B, Kim Y, Shaevitz JW, Petry S, Stone HA, Brangwynne CP. Capillary forces generated by biomolecular condensates. *Nature* 2022, **609**(7926)**:** 255-264.

11. Lipowsky R. Response of Membranes and Vesicles to Capillary Forces Arising from Aqueous Two-Phase Systems and Water-in-Water Droplets. *The Journal of Physical Chemistry B* 2018, **122**(13)**:** 3572-3586.

12. Mangiarotti A, Chen N, Zhao Z, Lipowsky R, Dimova R. Wetting and complex remodeling of membranes by biomolecular condensates. *Nature Communications* 2023, **14**(1)**:** 2809.

13. Yuan F, Alimohamadi H, Bakka B, Trementozzi AN, Day KJ, Fawzi NL, *et al.* Membrane bending by protein phase separation. *Proceedings of the National Academy of Sciences* 2021, **118**(11)**:** e2017435118.

14. Bergeron-Sandoval L-P, Kumar S, Heris Hossein K, Chang Catherine LA, Cornell Caitlin E, Keller Sarah L, *et al.* Endocytic proteins with prion-like domains form viscoelastic condensates that enable membrane remodeling. *Proceedings of the National Academy of Sciences* 2021, **118**(50)**:** e2113789118.

15. Mondal S, Narayan K, Botterbusch S, Powers I, Zheng J, James HP, *et al.* Multivalent interactions between molecular components involved in fast endophilin mediated endocytosis drive protein phase separation. *Nature Communications* 2022, **13**(1)**:** 5017.

16. Mondal S, Baumgart T. Membrane reshaping by protein condensates. *Biochimica et Biophysica Acta (BBA) - Biomembranes* 2023, **1865**(3)**:** 184121.

17. Lee Y, Park S, Yuan F, Hayden CC, Wang L, Lafer EM, *et al*. Transmembrane coupling of liquid-like protein condensates. *Nature Communications* 2023, **14**(1)**:** 8015.

18. Li Y, Lipowsky R, Dimova R. Transition from complete to partial wetting within membrane compartments. *Journal of the American Chemical Society* 2008, **130**(37)**:** 12252-12253.

19. Lu T, Liese S, Schoenmakers L, Weber CA, Suzuki H, Huck WTS, Spruijt E. Endocytosis of Coacervates into Liposomes. *Journal of the American Chemical Society* 2022, **144**(30)**:** 13451-13455.

20. Malacrida L. Phasor plots and the future of spectral and lifetime imaging. *Nature Methods* 2023, **20**(7)**:** 965-967.

21. Mangiarotti A, Dimova R. The spectral phasor approach to resolving membrane order with environmentally sensitive dyes. *Methods in Enzymology*. Academic Press, 2024.

22. Mangiarotti A, Siri M, Tam NW, Zhao Z, Malacrida L, Dimova R. Biomolecular condensates modulate membrane lipid packing and hydration. *Nature Communications* 2023, **14**(1)**:** 6081.

23. Chung JK, Huang WYC, Carbone CB, Nocka LM, Parikh AN, Vale RD, Groves JT. Coupled membrane lipid miscibility and phosphotyrosine-driven protein condensation phase transitions. *Biophysical Journal* 2021, **120**(7)**:** 1257-1265.

24. Cans AS, Andes-Koback M, Keating CD. Positioning lipid membrane domains in giant vesicles by micro-organization of aqueous cytoplasm mimic. *Journal of the American Chemical Society* 2008, **130**(23)**:** 7400-7406.

25. Andes-Koback M, Keating CD. Complete Budding and Asymmetric Division of Primitive Model Cells To Produce Daughter Vesicles with Different Interior and Membrane Compositions. *Journal of the American Chemical Society* 2011, **133**(24)**:** 9545-9555.

26. Su W-C, Ho JCS, Gettel DL, Rowland AT, Keating CD, Parikh AN. Kinetic control of shape deformations and membrane phase separation inside giant vesicles. *Nature Chemistry* 2023.

27. Babl L, Merino-Salomón A, Kanwa N, Schwille P. Membrane mediated phase separation of the bacterial nucleoid occlusion protein Noc. *Scientific Reports* 2022, **12**(1)**:** 17949.

28. Mangiarotti A, Bagatolli LA. Impact of macromolecular crowding on the mesomorphic behavior of lipid self-assemblies. *Biochimica et Biophysica Acta (BBA) - Biomembranes* 2021, **1863**(12)**:** 183728.

29. Socas LBP, Ambroggio EE. Linking surface tension to water polarization with a new hypothesis: The Ling-Damodaran Isotherm. *Colloids and Surfaces B: Biointerfaces* 2023, **230:** 113515.

30. Weber G, Farris FJ. Synthesis and spectral properties of a hydrophobic fluorescent probe: 6-propionyl-2-(dimethylamino)naphthalene. *Biochemistry* 1979, **18**(14)**:** 3075-3078.

31. Bagatolli LA. LAURDAN Fluorescence Properties in Membranes: A Journey from the Fluorometer to the Microscope. In: Mély Y, Duportail G (eds). *Fluorescent Methods to Study Biological Membranes*. Springer Berlin Heidelberg: Berlin, Heidelberg, 2013, pp 3-35.

32. Gunther G, Malacrida L, Jameson DM, Gratton E, Sánchez SA. LAURDAN since Weber: The Quest for Visualizing Membrane Heterogeneity. *Accounts of Chemical Research* 2021, **54**(4)**:** 976-987.

33. Parasassi T, De Stasio G, d'Ubaldo A, Gratton E. Phase fluctuation in phospholipid membranes revealed by Laurdan fluorescence. *Biophysical Journal* 1990, **57**(6)**:** 1179-1186.

34. Fereidouni F, Bader AN, Gerritsen HC. Spectral phasor analysis allows rapid and reliable unmixing of fluorescence microscopy spectral images. *Opt Express* 2012, **20**(12)**:** 12729-12741.

35. Malacrida L, Astrada S, Briva A, Bollati-Fogolín M, Gratton E, Bagatolli LA. Spectral phasor analysis of LAURDAN fluorescence in live A549 lung cells to study the hydration and time evolution of intracellular lamellar body-like structures. *Biochimica et Biophysica Acta (BBA) - Biomembranes* 2016, **1858**(11)**:** 2625-2635.

36. Golfetto O, Hinde E, Gratton E. The Laurdan Spectral Phasor Method to Explore Membrane Micro-heterogeneity and Lipid Domains in Live Cells. In: Owen DM (ed). *Methods in Membrane Lipids*. Springer New York: New York, NY, 2015, pp 273-290.

37. Socas LBP, Valdivia-Pérez JA, Fanani ML, Ambroggio EE. Multidimensional Spectral Phasors of LAURDAN's Excitation–Emission Matrices: The Ultimate Sensor for Lipid Phases? *Journal of the American Chemical Society* 2024, **146**(25)**:** 17230-17239.

38. Malacrida L, Gratton E, Jameson DM. Model-free methods to study membrane environmental probes: a comparison of the spectral phasor and generalized polarization approaches. *Methods and Applications in Fluorescence* 2015, **3**(4)**:** 047001.

39. Parasassi T, De Stasio G, Ravagnan G, Rusch RM, Gratton E. Quantitation of lipid phases in phospholipid vesicles by the generalized polarization of Laurdan fluorescence. *Biophysical Journal* 1991, **60**(1)**:** 179-189.

40. Gratton E, Digman MA. Laurdan identifies different lipid membranes in eukaryotic cells. In: Cambi A, Lidke DS (eds). *Cell Membrane Nanodomains: from Biochemistry to Nanoscopy*. CRC Press, 2014, p 510.

41. Torrado B, Malacrida L, Ranjit S. Linear Combination Properties of the Phasor Space in Fluorescence Imaging. *Sensors*; 2022.

42. Malacrida L, Ranjit S, Jameson DM, Gratton E. The Phasor Plot: A Universal Circle to Advance Fluorescence Lifetime Analysis and Interpretation. *Annual Review of Biophysics* 2021, **50**(1)**:** 575-593.

43. Lipowsky R. Remodeling of Biomembranes and Vesicles by Adhesion of Condensate Droplets. *Membranes* 2023, **13**(2)**:** 223.

44. Mangiarotti A, Dimova R. Biomolecular Condensates in Contact with Membranes. *Annual Review of Biophysics* 2024.

45. Chen N, Zhao Z, Wang Y, Dimova R. Resolving the Mechanisms of Soy Glycinin Self-Coacervation and Hollow-Condensate Formation. *ACS Macro Letters* 2020, **9**(12)**:** 1844-1852.

46. Lipowsky R. Spontaneous tubulation of membranes and vesicles reveals membrane tension generated by spontaneous curvature. *Faraday Discussions* 2013, **161:** 305-331.

47. Zhao Z, Roy D, Steinkühler J, Robinson T, Lipowsky R, Dimova R. Super-Resolution Imaging of Highly Curved Membrane Structures in Giant Vesicles Encapsulating Molecular Condensates. *Adv Mater* 2022, **34**(4)**:** 2106633.

48. Kusumaatmaja H, Li Y, Dimova R, Lipowsky R. Intrinsic Contact Angle of Aqueous Phases at Membranes and Vesicles. *Physical Review Letters* 2009, **103**(23)**:** 238103.

49. Parasassi T, Di Stefano M, Loiero M, Ravagnan G, Gratton E. Cholesterol modifies water concentration and dynamics in phospholipid bilayers: a fluorescence study using Laurdan probe. *Biophysical Journal* 1994, **66**(3, Part 1)**:** 763-768.

50. Mangiarotti A, Genovese DM, Naumann CA, Monti MR, Wilke N. Hopanoids, like sterols, modulate dynamics, compaction, phase segregation and permeability of membranes. *Biochimica et Biophysica Acta (BBA) - Biomembranes* 2019, **1861**(12)**:** 183060.

51. Gracià RS, Bezlyepkina N, Knorr RL, Lipowsky R, Dimova R. Effect of cholesterol on the rigidity of saturated and unsaturated membranes: fluctuation and electrodeformation analysis of giant vesicles. *Soft Matter* 2010, **6**(7)**:** 1472-1482.

52. Levental I, Levental KR, Heberle FA. Lipid Rafts: Controversies Resolved, Mysteries Remain. *Trends in Cell Biology* 2020, **30**(5)**:** 341-353.

53. Lee I-H, Imanaka MY, Modahl EH, Torres-Ocampo AP. Lipid Raft Phase Modulation by Membrane-Anchored Proteins with Inherent Phase Separation Properties. *ACS Omega* 2019, **4**(4)**:** 6551-6559.

54. Yoo BY, Chrispeels MJ. The origin of protein bodies in developing soybean cotyledons: a proposal. *Protoplasma* 1980, **103**(2)**:** 201-204.

55. Li Y, Lipowsky R, Dimova R. Membrane nanotubes induced by aqueous phase separation and stabilized by spontaneous curvature. *Proceedings of the National Academy of Sciences of the United States of America* 2011, **108**(12)**:** 4731-4736.

56. Liu Y, Agudo-Canalejo J, Grafmüller A, Dimova R, Lipowsky R. Patterns of Flexible Nanotubes Formed by Liquid-Ordered and Liquid-Disordered Membranes. *ACS Nano* 2016, **10**(1)**:** 463-474.

57. Schmidt ML, Ziani L, Boudreau M, Davis JH. Phase equilibria in DOPC/DPPC: Conversion from gel to subgel in two component mixtures. *The Journal of Chemical Physics* 2009, **131**(17)**:** 175103.

58. Aleksanyan M, Faizi HA, Kirmpaki M-A, Vlahovska PM, Riske KA, Dimova R. Assessing membrane material properties from the response of giant unilamellar vesicles to electric fields. *Advances in Physics: X* 2023, **8**(1)**:** 2125342.

59. Bassereau P, Jin R, Baumgart T, Deserno M, Dimova R, Frolov VA, *et al.* The 2018 biomembrane curvature and remodeling roadmap. *Journal of Physics D: Applied Physics* 2018, **51**(34)**:** 343001.

60. Karimi M, Steinkühler J, Roy D, Dasgupta R, Lipowsky R, Dimova R. Asymmetric Ionic Conditions Generate Large Membrane Curvatures. *Nano Letters* 2018, **18**(12)**:** 7816-7821.

61. Zhao Z, Satarifard V, Lipowsky R, Dimova R. Membrane nanotubes transform into double-membrane sheets at condensate droplets. *Proceedings of the National Academy of Sciences* 2024, **121**(26)**:** e2321579121.

62. Kusumaatmaja H, May AI, Knorr RL. Intracellular wetting mediates contacts between liquid compartments and membrane-bound organelles. *Journal of Cell Biology* 2021, **220**(10)**:** e202103175.

63. Dimova R, Lipowsky R. Giant Vesicles Exposed to Aqueous Two-Phase Systems: Membrane Wetting, Budding Processes, and Spontaneous Tubulation. *Advanced Materials Interfaces* 2017, **4**(1)**:** 1600451.

64. Steinkühler J, Sezgin E, Urbančič I, Eggeling C, Dimova R. Mechanical properties of plasma membrane vesicles correlate with lipid order, viscosity and cell density. *Communications Biology* 2019, **2**(1)**:** 337.

65. Mangiarotti A, Aleksanyan M, Siri M, Sun T-W, Lipowsky R, Dimova R. Photoswitchable Endocytosis of Biomolecular Condensates in Giant Vesicles. *Advanced Science* 2024, **n/a**(n/a)**:** 2309864.

66. Orlikowska-Rzeznik H, Versluis J, Bakker HJ, Piatkowski L. Cholesterol Changes Interfacial Water Alignment in Model Cell Membranes. *Journal of the American Chemical Society* 2024.

67. Vallmitjana A, Lepanto P, Irigoin F, Malacrida L. Phasor-based multi-harmonic unmixing for in-vivo hyperspectral imaging. *Methods and Applications in Fluorescence* 2023, **11**(1)**:** 014001.

68. Last MGF, Deshpande S, Dekker C. pH-Controlled Coacervate–Membrane Interactions within Liposomes. *ACS Nano* 2020, **14**(4)**:** 4487-4498.

69. Yuan F, Lee CT, Sangani A, Houser JR, Wang L, Lafer EM, *et al.* The ins and outs of membrane bending by intrinsically disordered proteins. *Science Advances*, **9**(27)**:** eadg3485.

70. Melia TJ, Lystad AH, Simonsen A. Autophagosome biogenesis: From membrane growth to closure. *Journal of Cell Biology* 2020, **219**(6)**:** e202002085.

71. Shibata Y, Voeltz GK, Rapoport TA. Rough Sheets and Smooth Tubules. *Cell* 2006, **126**(3)**:** 435-439.

72. Mondal S, Cui Q. Coacervation-Induced Remodeling of Nanovesicles. *The Journal of Physical Chemistry Letters* 2023, **14**(19)**:** 4532-4540.

73. Mondal S, Cui Q. Sequence Sensitivity in Membrane Remodeling by Polyampholyte Condensates. *The Journal of Physical Chemistry B* 2024, **128**(9)**:** 2087-2099.

74. Shillcock JC, Thomas DB, Beaumont JR, Bragg GM, Vousden ML, Brown AD. Coupling Bulk Phase Separation of Disordered Proteins to Membrane Domain Formation in Molecular Simulations on a Bespoke Compute Fabric. *Membranes*; 2022.

75. Mangiarotti A, Wilke N. Electrostatic interactions at the microscale modulate dynamics and distribution of lipids in bilayers. *Soft Matter* 2017, **13**(3)**:** 686-694.

76. Angelova MI, Soléau S, Méléard P, Faucon F, Bothorel P. Preparation of giant vesicles by external AC electric fields. Kinetics and applications. In: Helm C, Lösche M, Möhwald H (eds). *Trends in Colloid and Interface Science VI*, vol. 89. Steinkopff, 1992, pp 127-131.

77. Weinberger A, Tsai FC, Koenderink GH, Schmidt TF, Itri R, Meier W, *et al.* Gel-Assisted Formation of Giant Unilamellar Vesicles. *Biophysical Journal* 2013, **105**(1)**:** 154-164.

78. Leung SSW, Brewer J, Bagatolli LA, Thewalt JL. Measuring molecular order for lipid membrane phase studies: Linear relationship between Laurdan generalized polarization and deuterium NMR order parameter. *Biochimica et Biophysica Acta (BBA) - Biomembranes* 2019, **1861**(12)**:** 183053.

79. Foley EDB, Kushwah MS, Young G, Kukura P. Mass photometry enables label-free tracking and mass measurement of single proteins on lipid bilayers. *Nat Methods* 2021, **18**(10)**:** 1247-1252.

## Acknowledgements

A.M. acknowledges support from Alexander von Humboldt Foundation. Authors would like to acknowledge Dr. Helge Ewers for the support with mass photometry experiments.

## Contributions

A.M. and R.D. conceived the experiments and designed the project. R.D. supervised the project. R.L developed the theoretical framework. A.M. performed most of the experiments. K.V.S. performed mass photometry experiments. A.M. and K.V.S. analyzed the data. A.M. and R.D. wrote the paper, with input from the rest of the authors.